2013

AUTOMATED MIDLINE SHIFT DETECTION ON BRAIN CT IMAGES FOR COMPUTER-AIDED CLINICAL DECISION SUPPORT

Xuguang Qi
Virginia Commonwealth University

AUTOMATED MIDLINE SHIFT DETECTION ON BRAIN CT IMAGES

FOR COMPUTER-AIDED CLINICAL DECISION SUPPORT

AUTOMATED MIDLINE SHIFT DETECTION ON BRAIN CT IMAGES

FOR COMPUTER-AIDED CLINICAL DECISION SUPPORT

A research dissertation submitted in partial fulfillment of the requirements for the degree of Dorctor of Philosophy at Virginia Commonwealth University

by

XUGUANG QI

Doctor of Philosophy in Computer Science
School of Engineering

Director: Assoc. Prof. Kayvan Najarian
Department of Computer Science

Virginia Commonwealth University
Richmond, VA
May 2013

Acknowledgement

I deeply appreciate the people who have been supporting and helping me in different ways throughout the entire process of my doctoral studies as well as completing this dissertation. First of all, I would like to express my deepest gratitude to my academic advisor, Dr. Kayvan Najarian, for his continuous support and guidance on this program. During these years in my program, he continuously shared his insights and helped me with his ideas. I also appreciate the help and support from Sharad Shandilya, Dr. Wenan Chen, and Dr. Ashwin Belle; in particular for many useful research discussions I had with them. Special thanks to Dr. Yang Tang M.D. for professional clinical suggestions and his clinical interpretation of images. I would also like to acknowledge Dr. Rosalyn S Hobson, Dr. Meng Yu, Dr. Alen Docef, Dr. Wanyu Zang, and M.D. Kevin Ward for their helpful advice and support. I am indebted to Dr. Marcel P Jackowski in University of São Paulo for providing very helpful suggestions and advice. In addition I would like to thank Sardar Ansari, Dr. Yurong Luo, Dr. Jie Wu, Leila Ghaedi, Mahsa Zahery, Michael

Pfaffenberger, Machel Roberts and Eric Myer and all other friends and member of Biomedical Signal and Image Processing Lab. The generous assistance from them and the pleasant cooperation with them was one of the most important reasons for enabling me to complete this work.

Most importantly, I would like to offer my special thanks to my parents for their endless love and concern. Most of all, I would especially thank my dear wife, Dr. Hongrui Liu, for her everlasting love and encouragement as well as the most reliable support. This work would not have been possible without her.

Table of Contents

List of Tables

List of Figures

Abstract

AUTOMATED MIDLINE SHIFT DETECTION ON BRAIN CT IMAGES FOR COMPUTER-AIDED CLINICAL DECISION SUPPORT

By Xuguang Qi

A research dissertation submitted in partial fulfillment of the requirements for the degree of Dorctor of Philosophy at Virginia Commonwealth University

Virginia Commonwealth University, 2013

Major Director: Kayvan Najarian, Associate Professor, Dept. Computer Science

Midline shift (MLS), the amount of displacement of the brain's midline from its normal symmetric position due to illness or injury, is an important index for clinicians to assess the severity of traumatic brain injury (TBI).

In this dissertation, an automated computer-aided midline shift estimation system is proposed. First, a CT slice selection algorithm (SSA) is designed to automatically select a subset of appropriate CT slices from a large number of raw images for MLS detection. Next, ideal midline detection is implemented based on skull bone anatomical features and global rotation assumptions. For the actual midline detection algorithm, a window

selection algorithm (WSA) is applied first to confine the region of interest, then the variational level set method is used to segment the image and extract the ventricle contours. With a ventricle identification algorithm (VIA), the position of actual midline is detected based on the identified right and left lateral ventricle contours. Finally, the brain midline shift is calculated using the positions of detected ideal midline and actual midline.

One of the important applications of midline shift in clinical medical decision making is to estimate the intracranial pressure (ICP). ICP monitoring is a standard procedure in the care of severe traumatic brain injury (TBI) patients. An automated ICP level prediction model based on machine learning method is proposed in this work. Multiple features, including midline shift, intracranial air cavities, ventricle size, texture patterns, and blood amount, are used in the ICP level prediction. Finally, the results are evaluated to assess the effectiveness of the proposed method in ICP level prediction.

Novelty and Contribution

Medical data acquired practically all clinical settings contains massive amount of information but not all of this information may be relevant to a specific medical decision making process. Often simple visual inspection and traditional computational methods are incapable of extracting the hidden information behind the preliminary data, which may be instrumental in generating recommendations and predictions for both diagnosis and treatment planning. Midline shift (MLS) estimation is a vital step in clinical decision making for patients with traumatic brain injury (TBI). Computer-aided midline shift detection is crucial to assist physicians make an accurate diagnosis on the severity of TBI within a reasonable time.

In this work, an automated MLS estimation system with high accuracy is proposed to quantitatively analyze the severity of the brain injury. Using machine learning, ICP is predicted as the reference of physician decision making. This machine learning model is trained and tested using a nested crossing validation process. Novelties provided by this research include:

- **Automated CT slice selection**

Numerous raw CT slices can be acquired from one scan but not all slices are suitable for the midline shift detection. In clinical setting, physician manually chooses a few slices for diagnosis. In this work, a CT slice selection algorithm (SSA) is designed to perform the automated slice selection process in order to obtain the most suitable slices for MLS estimation. During the slice selection process, the proposed SSA algorithm automatically considers multiple anatomic information of the human brain, including the expected skull

appearance, the proper representation of intracranial region, and the topology of the ventricle system. With the significant reduction in the number of candidate slices considered for the MLS detection, the computation time needed to process the following steps is dramatically reduced.

- **Ideal midline detection system**

Fully considering the symmetry of the skull and anatomical features, the proposed ideal midline detection algorithm is designed to accurately identify the ideal midline on the candidate CT slices selected by the SSA algorithm. It contains two continuous processes, both of which have the assistance of the global rotation. The application of global rotation ensures accurate ideal midline detection. Exhaustive symmetric position search algorithm is used to detect the approximate ideal midline based on the row symmetry cost. Subsequently, a multiple segmentation methods based on the brain anatomical features are utilized to refine the ideal midline. Finally the brain direction is calibrated by making the detected ideal midline in vertical direction.

- **Dynamic window selection**

In order to further reduce the computation time involved in searching for the actual midline, a dynamic window selection method is designed by confining the region of interest in this work. Window selection algorithm (WSA) is proposed to fulfill this task on the slices selected by the SSA algorithm. The WSA algorithm not only narrows down the search for the most suitable CT slice but also confines the window in which the ventricles reside. The selected window is used as the initialization of the level set

segmentation. This process by itself can be used in other brain image processing applications as well as other similar applications.

- **Segmentation based on the variational level set model**

Level set method is a popular deformation model in medical image processing. Variational level set segmentation applied in this work, is a modified level set method that is designed to resolve the re-initialization limitations of the original method and reduce its sensitivity to intensity inhomogeneity of the image. In our system, the variational level set segmentation model combined with the ventricle identification process successfully extracts the contours of ventricles. Actual midline is estimated by the positions of the ventricle contours.

Compared with other segmentation methods that have been used in the MLS detection, such as the Gaussian Mixture Model (GMM), the variational level set model has proved to successfully reduce the time consumption and effectively enhance the accuracy of the segmentation.

- **MLS application: ICP prediction**

One of the important applications of midline shift in medical diagnosis is intracranial pressure (ICP) prediction. Elevated ICP may results in secondary complications or death via swelling and deformation of the brain tissues.

In this work, an ICP level prediction model is designed, by applying machine learning on multiple features extracted from brain CT images, including the estimated midline shift. Other features extracted from CT are included in the prediction process include

intracranial air cavities, ventricle size, texture patterns and blood amount. These features are added to other information such as demographics as important features and are used in the prediction process. The obtained results show that the proposed model can potentially be applied towards developing a clinically-useful pre-screening system for detection of elevated ICP.

Chapter 1: Introduction

1.1 Motivation and background

1.1.1 Brain midline shift and its medical applications

In the United States, nearly 1.7 million cases of traumatic brain injury (TBI) are recorded annually, among which 1.365 million, i.e. nearly 80% of all cases are treated and released from an emergency department, 275,000 are hospitalized, and 52,000 die [1]. It has to be added that 26,000 lose their lives in the first two hours after injury. The majority of TBI survivors may suffer from significant physical health problems including permanent disability, which may seriously affect their lives as well as the lives of their families in both emotional and financial aspects [2, 3, 4]. TBI is considered as one of the leading causes of the death in children and young adults [5, 6]. An accurate medical diagnosis at the time of injury or soon after may dramatically alleviate the complications, avoid lifelong disability, or even save life [7, 8]. Thus, fast and accurate diagnosis is vital in TBI care.

One of the most serious problems associated with TBI is the elevation of intracranial pressure (ICP), which could lead to the deformation of brain tissue and ventricular structure thereby further complicating the injury and causing secondary complications [5]. Although invasive direct monitoring of ICP through cranial trepanation is an option to detect ICP level and its potential elevation, this invasive procedure could sometimes cause further complications [9]. Therefore, a non-invasive and cost-effective pre-

screening method to estimate ICP levels and potentially eliminate the need for invasive monitoring at least in a portion of patients would be highly desirable.

A CT scan is usually taken soon after TBI in emergency medical practice. The tissue shift and deformation shown in the scan is a vital reference for physician in medical diagnosis. One of the potential deformations, the brain midline shift (MLS), is an important index for clinicians to assess the severity of TBI and is known to be highly correlated with the ICP levels [9]. MLS greater than 5 mm can lead to sufalcine herniation and possibly death [10].

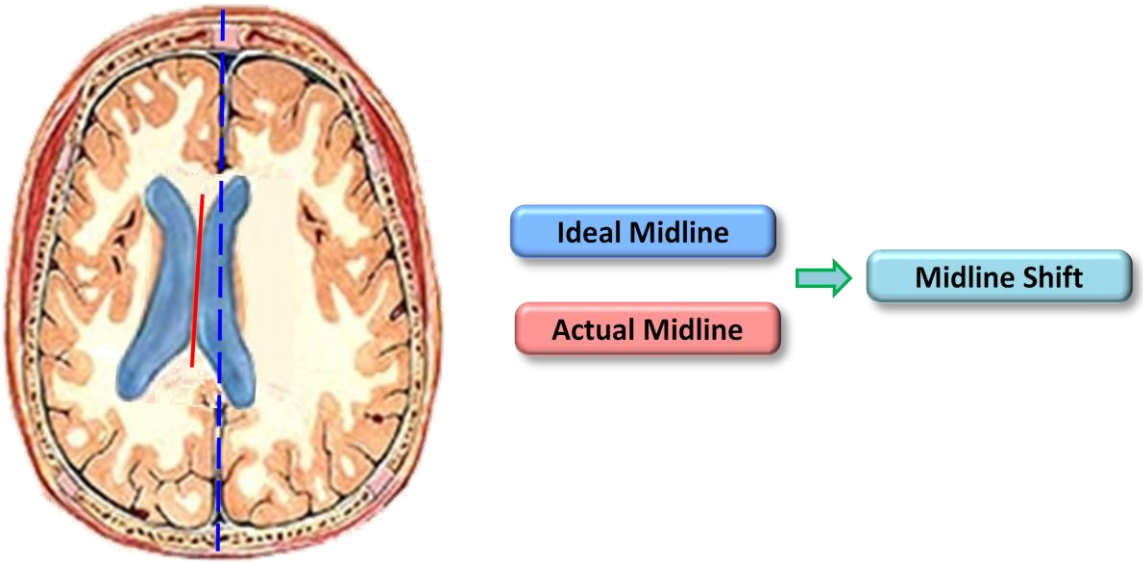

Figure 1.1 Brain midline shift. Blue dash line represents the ideal midline and red solid line represents the shifted actual midline [11].

The Midline Shift (MLS) is the degree of shift in the brain, measured roughly at about the center of the brain, which is caused by the injury or illness. As shown in Figure 1.1, the detection of MLS often involves the following two main steps: estimation of ideal midline (symmetric midline as if the injury or illness had not occurred) and detection of

actual midline (shifted midline after injury or illness). Since the ideal midline is used as reference in the MLS detection, the ideal midline estimation significantly affects the accuracy of the MLS detection. The actual midline usually is detected using the anatomic information of the brain after the injury or illness. This anatomical information includes the position of the ventricle system, which is the key clinical factor in identifying where the line resides.

1.1.2 Computed Tomography (CT) technique

Figure 1.2 CT scanner (Toshiba's High-Powered CT scanner) [12]

Computed Tomography (CT) is used in the estimation of MLS in this work, while other image modalities such as MRI could have been applied in this study as well. However, the CT is more practical system for initial TBI assessment due to its fast speed, lower

cost and high quality, and as a result, in practically all emergency medicine settings CT is the standard imaging technology used for assessment of TBI, at least for the initial assessment [13]. In addition, modern CT scanner can acquire high quality non-contrast brain CT scan in less than 10 seconds. CT scan is considered as a golden standard in assessment for acute hemorrhage and very desirable at documenting mass effect and herniation as well as effective at visualizing skull fracture [10].

As one of the important medical imaging method, CT utilizes tomography methods [14] and can provide high resolution images showing serious lesions such as intracranial hematoma, hemorrhage, and brain contusions [15]. From the emergence of CT scanning in medicine in 1970s, CT has provided the possibility of quick diagnosis of ongoing intracranial damage and the possible neurosurgical intervention afterward, which is the key to overcome life threatening events in head injured patients [16-19].

The size and number of pixels in CT image depend on the setting of the CT scanner. Smaller size of pixels combined with each other builds up higher resolution image.

In CT image, the dark regions represent the tissue with a low absorption of X-ray, such as air or ventricular system in brain, while the bright regions represent the area with high absorption of X-ray, such as bone or blood. CT value measured in Hounsfield Unit (Hu) is used to describe the density of pixels in CT image. Different tissues in human body have different densities with the CT values range from -1000 Hu to 3000 Hu except for very dense materials such as dental fillings or metal implants [20]. For example, the CT value is -1000 Hu for air, -400 to -600 Hu for lung tissue, -60 to 100 Hu for fat tissue, 0 Hu for water, 40 to 80 Hu for soft tissue, and 400 to 1000 Hu for bone. Figure 1.2 is an example of CT imaging devices. Figure 1.3 shows a sample of the brain CT image.

Figure 1.3 A sample of brain CT image

1.1.3 Ventricle system in the human brain

The ventricles of the brain form a connected network of cavities filled with cerebrospinal fluid (CSF) and located within the brain parenchyma (Figure 1.4). The ventricular system is composed of two lateral ventricles (the left and right lateral ventricles), the third ventricle, the cerebral aqueduct, and the fourth ventricle [21]. The lateral ventricles are in the cerebral hemispheres. The lateral ventricles communicate with the third ventricle through the interventricular foramen. The third ventricle is a median cavity in the brain, bounded by the thalamus and hypothalamus on either side. In front, the third ventricle communicates with the lateral ventricles, and in back it communicates with the aqueduct of the midbrain. The fourth ventricle is the most inferior of the four ventricles of the brain

[22]. Since the left and right lateral ventricles can be easily displayed in the CT images, in this work, these two ventricles are used in the actual midline detection. In the normal brain of a young adult, the right and left lateral ventricles are symmetrically located in the two hemispheres. As a result of an illness or injury, the shifted ventricles position could provide a reference for the actual midline estimation. However, it is worth noticing that due to the complexity of the brain CT, the full size and position of the ventricles may not be fully reflected in some CT slices correctly. Therefore, the MLS diagnosis based on the position of ventricles must be implemented on a suitable slice, which contains the clearest and the most representative ventricle information.

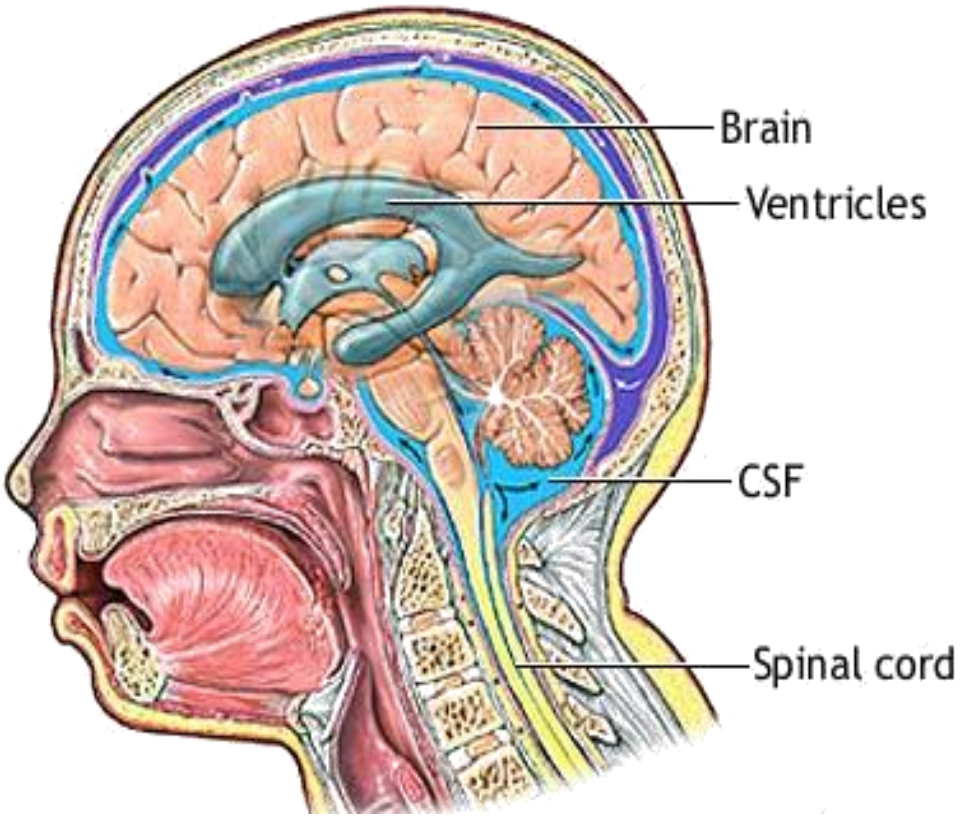

Figure 1.4 The ventricle system in the brain [23]

1.1.4 Automated computer aided clinical decision support systems

Automated computer aided clinical decision support systems have been proven as vital supportive tools for physicians in clinical practice. In clinic setting, physicians usually have to process lots of information in a short period of time and give accurate diagnosis so as to provide the best care to patients. In environments such as battlefield hospitals or emergency rooms, the number of patients may abruptly increase and might end up over burdening the physicians. Also, in the case of critical injuries where time is of essence, it is vital that physicians make accurate but swift diagnostic decisions so as to be able to provide required treatment(s) in time in order to save the patient's life. The large amount of patient's data presented to physicians, including CT scans, demographics and patient history, might require a lot of time to analyze. Under such critical situations, the automated computer-aided clinical decision support system could provide reliable recommendations for the physicians while effectively accelerate the decision making.

On the other hand, there is tremendous variety as well as complexity in the clinical data used for trauma care, it is challenging to avoid mis-diagnosis even for experienced trauma care professionals [24-27]. Other reasons for mis-diagnosis include unstable patients, incomplete medical records or complicating diseases [28-30]. Insufficient data analysis, limited time, and interference caused by fatigue all possibly lead to human error in the physician's mis-diagnosis. An automated computer-assisted decision support system could greatly help process all available patient information in a short time and give recommendations to physicians.

Automated midline shift detection on CT image is very challenging due to the injury severity, variation in the size, shape and location of ventricles from patient to patient, presence of image noise. There is a need to design an automated midline shift detection system on CT images towards providing recommendations to physicians in medical decision support in clinical practice.

1.1.5 Medical image segmentation

Image segmentation plays a significant role in the computer-aided medical images processing [31]. In computer vision, image segmentation is the process of partitioning a digital image into multiple regions (sets of pixels). The purpose of segmentation is to represent an image using a more simple and meaningful expression for analysis [32]. Image segmentation is typically used to locate objects and boundaries in image. Specifically, image segmentation is the process to assign a label on every pixel in an image such that pixels with the same label are connected, and the resulting collection of pixels shares certain visual characteristics. Pixels in one region in segmentation are similar with respect to some features, such as color, intensity, or texture. Adjacent regions may be significantly different with respect to the same characteristics [33].

Image segmentation algorithms have been applied to many biomedical applications such as quantification of tissue volumes [34], diagnosis [35], localization of pathology [36], study of anatomical structure [37], treatment planning [38], partial volume correction of functional imaging data [39], and computer integrated surgery [40, 41]. However, there is no gold-standard segmentation method which can satisfy the requirements of all medical imaging application. Methods aimed at particular applications can usually achieve better

performance by taking into account prior knowledge on a gray level appearance or shape characteristics. Segmentation techniques often have to be combined with domain knowledge in order to effectively solve the specific problems [42].

Image segmentation methods can be divided into three categories depending on the classification scheme, imaging modality, and specific application [42]:

- Manual, semiautomatic, and automatic
- Pixel or region based (including threshold method, region growing method, edge-based method), knowledge model based (including expectation maximization algorithm, Bayesian prior model), and deformable model based (including snakes, level set method)
- Classical (including threshold method, edge-based method, region growing method), fuzzy clustering, statistical atlas mapped, and neural network techniques.

Several medical image segmentation methods have attracted a great deal of attention in the last 2-3 decades. Here, we introduce several popular segmentation methods as follows.

1.1.5.1 Threshold method

Threshold based image segmentation method is usually as effective and popular method in image processing [43]. The setting of the threshold value is the key in this method. Using a fixed global threshold value for all examination is easier but may not able to provide consistent results for all cases. The popular Otsu method is a good example of utilizing global threshold method but fails for images containing non-uniform intensity changes. Using the local threshold values the inhomogeneous intensity can be factored in although the multi-threshold selection complicates the problem [43]. Although threshold

method is intuitive and fast, it is usually challenging, if not practical, to accurately segment regions of interest from complicated medical images such as the brain CT scans.

1.1.5.2 Region growing

Region growing is a technique for extracting a connected region of an image based on a predefined criterion [44, 45]. In this method, a see point or a set of seed points is selected initially and all the pixels around it are added based on some predefined criteria to the region represented by the seed [46, 47]. The seed initialization step, which is required for every region of interest, can be achieved by manual, semi automated, or fully automated processes. However, this method suffers from the hard definition of an appropriate seed setting. The accuracy of this method depends heavily on the chosen criteria. Region growing methods are simple techniques that provide relatively good results especially with smaller region segmentation in applications where the above-mentioned challenges can be properly addressed.

1.1.5.3 Clustering

Clustering methods partition data given image into a certain number of groups/clusters. These techniques are unsupervised techniques that iteratively alternate between segmenting the image and characterizing the properties of each cluster. Some clustering method, such K-mean segmentation [48], fuzzy-c-mean algorithm [49], and the expectation-maximization algorithm [49, 50] have become more popular in the medical image applications. The choice of similarity measure is the crucial aspect of the

clustering methods. However, it is difficult to directly incorporate spatial modeling and avoid effect of some inherent noise in the segmentation.

1.1.5.4 Classifiers

Classification methods usually apply a set of features or parameters, which should be relevant to the object being separated and use a classifier via a supervised learning task The training set is used by the classification programs to learn how to classify objects. In the training phase, the training set is used to determine how the parameters should be weighted and combined in order to separate the various regions/classes/objects. In the test phase, the parameters and their weights, determined during the training phase, are applied to determine their class and therefore segment the image [51]. The current popular classification methods used for segmentation include Gaussian Mixture Model (GMM) [52-54], Nearest-neighbor classifier [55], k-nearest-neighbor classifier [56], and maximum likelihood [57].

1.1.5.5 Deformable models

In the recent decades of years, deformable models have been widely used in medical image segmentation. Deformable models are curves or surfaces, defined within an image domain which can be moved by both internal forces and external forces. The internal forces defined within the curve or surface are aimed at keeping the model smooth during deformation, while the external forces computed from the image data are defined to move the model toward an object boundary or other desired features within an image.

Deformable models offer robustness to both image noise and boundary gaps. They also combine boundary elements into a coherent and consistent status. Such a boundary description can then be readily used by subsequent applications. In addition, since deformable models are implemented on the continuum, the resulting boundary representation can achieve subpixel accuracy, which is a highly desirable property for medical imaging applications [58]. The deformable methods can be categorized into three groups: parametric deformable models, geometric deformable models, and extensions of deformable models. The level set method used in this work is one popular method belonging to the geometric deformable method category.

1.2 System validation methods

Generally, the evaluation methods of image segmentation can be partitioned based on the methodologies used at five levels [59-62], as shown in Figure 1.5. The two main categories are subjective vs. objective evaluation, where subjective evaluation is made only by expert/evaluator examiners who investigate the segmentation results visually. The objective evaluation is further divided into system-level evaluation in which the segmentation considers the entire system/framework/application, and the direct evaluation in which the focus is only on the segmentation method itself. The direct objective evaluation contains the analytical methods and empirical methods which are either unsupervised or supervised depending on whether or not the method requires a ground-truth reference image. While every evaluation method has its own merit, the combination of the system-level evaluation and supervised evaluation forms the most popular approach in image processing systems [63, 64].

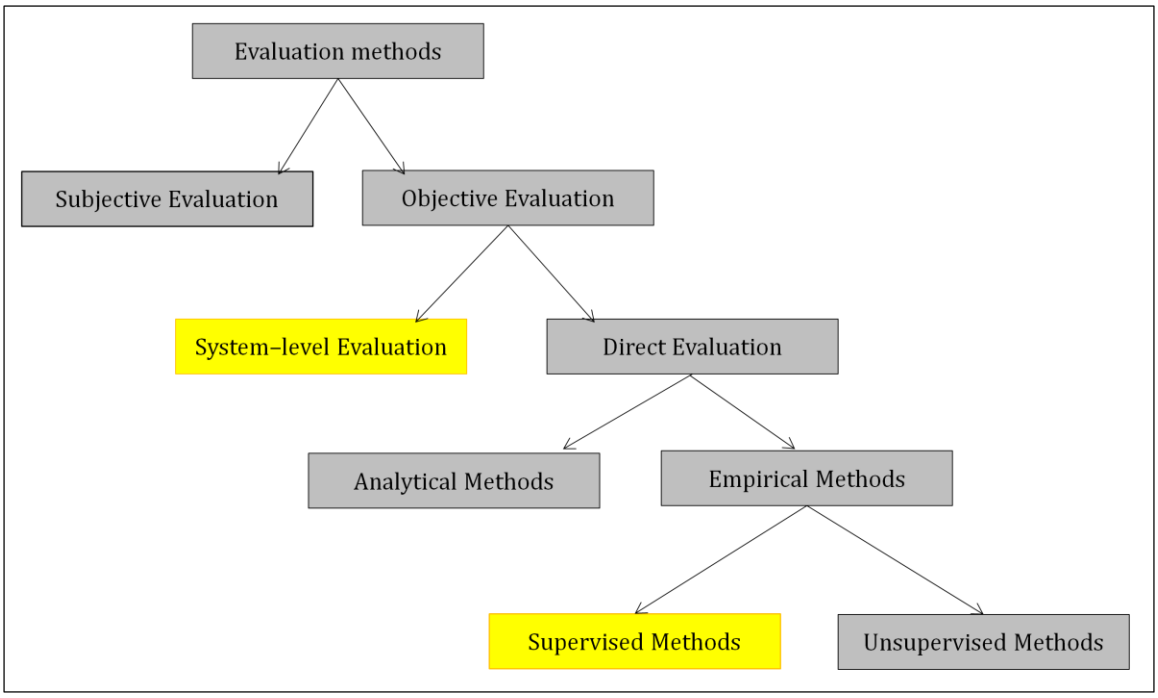

Figure 1.5 Hierarchy of segmentation evaluation methods. The highlighted evaluation methods will be applied on our proposed system.

Supervised evaluation methods (also called relative evaluation methods) [65-67] compare the segmentation obtained by a specific method against a manual segmentation operated by experts. The manual segmentation is considered as a ground-truth or gold standard in practice [60, 68]. The quantitative assessment of segmentation describes the degree of similarity between computer segmented images and reference images.

The supervised evaluation usually uses the discrepancy methods to objectively assess the quality of segmentation [59]. There are a variety of discrepancy measures. Some are based on the number of misclassified pixels to the reference image [69-73] while others are defined using the difference in the feature values of the segmented and reference

images [74-78]. In addition, some variational discrepancy methods are also applied in the segmentation evaluation [79-81]. One suitable discrepancy measure belonging to the first group is mis-segmentation measure, which is defined based on the mis-segmented areas, and has proved to be a successful measure in evaluating segmentation methods [82].

In this work, the system-level evaluation and supervised evaluation methods using multiple measures is applied to assess the efficiency and accuracy of the ventricle segmentation and the midline shift detection. In addition, the decision making / prediction methods, such ICP prediction methods, are also qualitatively assessed using the same approach.

1.3 Proposed method

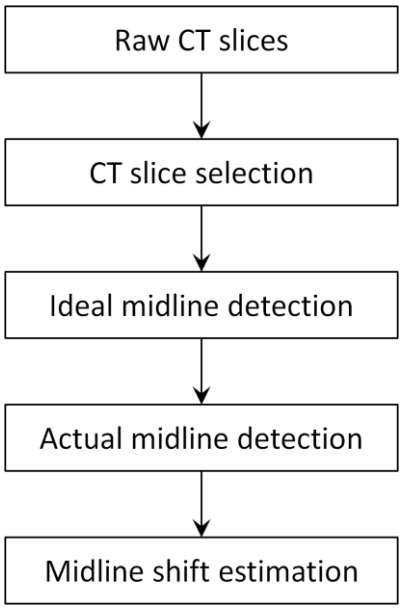

Figure 1.6 Schematic diagram of the overall system

The overall system is a four-step process that estimates the brain midline shift as shown in schematic diagram of Figure 1.6. As the first step, a CT Slice Selection Algorithm is used, wherein the algorithm finds a suitable subset of slices from a large number of raw CT images. In the second step, the ideal midline of the brain is accurately and effectively detected by considering both anatomical features and the overlapping information among the CT slices. In this step, the algorithm not only recognizes the ideal midline, which can be used as a reference for the comparison in the final MLS calculation, but also centralizes the CT images. In the third step, the actual midline detection begins with our novel Window Selection Algorithm designed to narrow the focus only to the regions of interest and subsequently uses level set segmentation to extract the ventricle contours. Using the position of the detected left and right lateral ventricles, the actual midline is identified on the brain CT image. At last, the brain midline shift is estimated by the distance between the detected ideal midline and actual midline.

The rest of the dissertation is organized as follows. In Chapters 2 to 4, we illustrate the SSA algorithm, ideal midline detection, actual midline detection and the MLS calculation. Chapter 5 introduces the medical application of brain midline shift. Chapter 6 summarizes our work.

Chapter 2 CT Slice Selection Algorithm

2.1 Background and introduction

In clinical settings, although several different levels of CT images can be acquired in the head CT scans of one patient, only those slices clearly showing ventricles are valuable in the midline shift estimation. Moreover, noise and interference in some images may seriously affect the usability of the ventricle structure in these images. In addition, clinically speaking, it is neither necessary nor desired to detect midline shift on all CT slices. Therefore, the first step in automated midline shift detection is to select the most appropriate CT slices to process the detection.

Currently in clinical practice, the process of slice selecting for MLS diagnosis is performed manually by physicians [9, 83]. Physician visually inspects all valuable information for MLS diagnosis in all slices, including scan position, skull shape, ventricular structure, and the image clarity, and then selects a few appropriate slices for further diagnosis. To closely simulate the physician's operation, the first step in the computer aided brain midline shift detection should be an automated slice selection process. In addition, this process dramatically reduces the computation time by limiting the image processing only on a few slices. We did not find any existing automated method to perform this task.

In this work, a novel algorithm called CT Slice Selection Algorithm (SSA) has been developed, to fulfill this requirement and subsequently provide a prerequisite for achieving the fully automatic MLS detection. The rest of this chapter is organized as

follows: the methodology is introduced in Section 2.2, results are presented and discussed in Section 2.3, and the Chapter is summarized in Section 2.4.

2.2 Methodology

With head CT scan in the clinical environment, dozens of raw images can easily be acquired for one patient. However, not all images are ideal for IML detection. As shown in Figure 2.1, there are 42 raw CT images obtained from one patient's CT scan. Some images taken from the lower section of the head contains too much noise/interference from other organs, such as the eye and nose in slice No.15. Some images capture only a small intracranial area because the scan position is too close to the calvaria, as seen in slice No.36; some images capture closed skull contours and large intracranial area but lack good convexity there rendering them improper for midline detection, such as slice No.19; some images with good skull contour and large intracranial area have too little ventricle information for MLS detection, such as slice No.31. From the viewpoint of anatomical features, ideal CT slices for MLS estimation should contain larger intracranial area, closed skull bone contour, good convexity of the skull, and clear ventricle tissue, such as No.22 through No.30 in Figure 2.1. Therefore, the CT slice selection should be based on the above mentioned features and requirements.

To effectively select a few appropriate CT slices from a large number of CT scan images acquired for each patient, the CT Slice Selection Algorithm (SSA) was proposed. As the flowchart shows in Figure 2.2, this algorithm analyzes every slice by examining multiple anatomic features. Raw CT slice is examined by skull detection, closed skull inspection, intracranial area detection, convexity inspection, and ventricle visibility identification.

Each aspect of the flowchart has been described in the following sections. Among them, the last step, ventricle visibility identification, needs multiple detail steps for implementation which are introduced in Section 2.2.5.

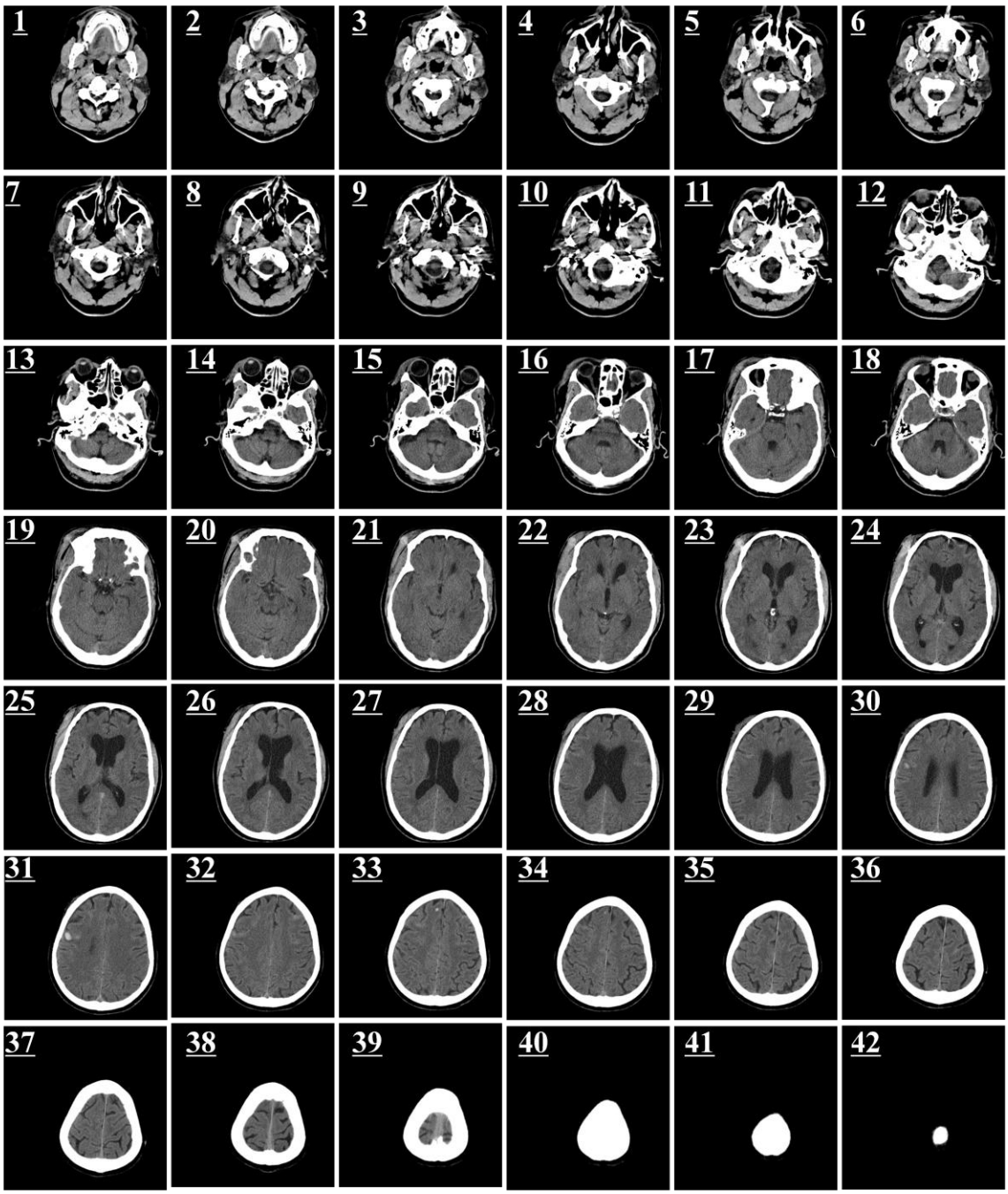

Figure 2.1 Raw CT slices from one patient's head CT scan.

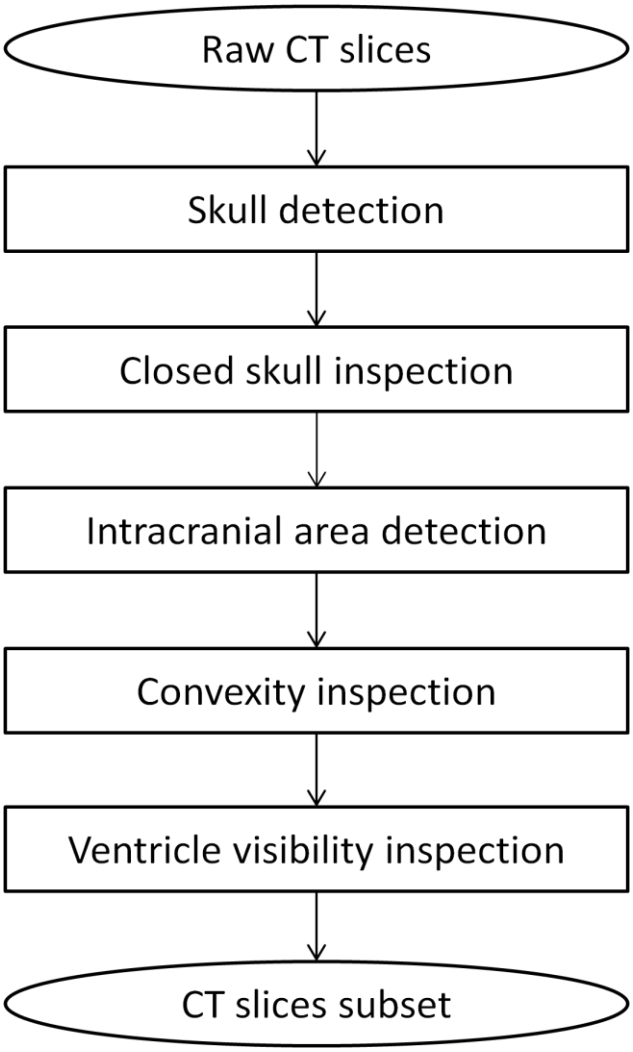

Figure 2.2 Schematic diagram of CT Slice Selection Algorithm (SSA)

2.2.1 Skull detection

As the first step in SSA algorithm, the skull detection is firstly implemented on every raw CT slice as shown in Figure 2.3. In this step a raw CT image is treated as a raw matrix *I* with *m* rows and *n* columns (Eq. 2-1).

$$I = (I_{i,j}) \quad (i = 1, \dots, m \; and \; j = 1, \dots, n) \qquad \text{Eq. 2-1}$$

where I_{ij} represents the intensity of the pixel at the *i*th row and *j*th column. Using a threshold method, the possible bone pixels can be extracted from the raw matrix to build up a new binary matrix *B* as shown in Figure 2.3-b.

$$B = (B_{i,j}) \; (i = 1, \dots, m \; and \; j = 1, \dots, n) \qquad \text{Eq. 2-2}$$

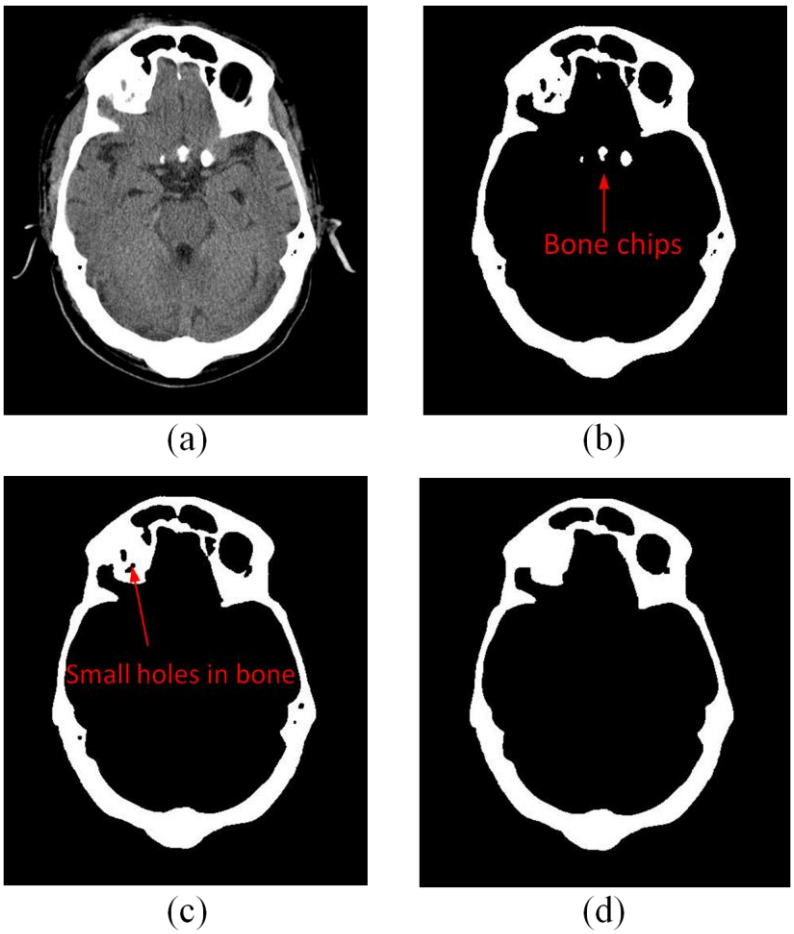

Figure 2.3 Skull detection process on a CT slice (a) Raw CT slice, (b) the detected bones *B* by the threshold method. Bone chips and small holes inside bone region are all detected, (c) the candidate skull bone C_a after removing small bone chips, (d) the detected skull

where the pixels with their original intensity I_{ij} is larger than the threshold of T. In this study, based on experimentation, the value for T is set to 250 (out of 255), which lies within the common range for bone intensity within CT images. (See Eq. 2-3).

$$B_{ij} = \begin{cases} 1, & if\ I_{ij} > T \\ 0, & else \end{cases} \quad (i = 1, \dots, m\ and\ j = 1, \dots, n) \qquad \text{Eq. 2-3}$$

where, B_{ij} is the element at *i*th row and *j*th column in the new binary matrix *B*. Then those possible bone pixels constitute a certain number of connected regions $C_1, C_2, \dots, C_p$ by means of the connected component algorithm (CCA) [84]. We choose the *a*th connected region C_a *(1≤a≤p)* which contains the largest number of elements as the candidate skull as shown in Eq. 2-4.

$$C_a = \arg\max_{C_k}[\, f(C_1), f(C_2), \cdots f(C_p)] \qquad \text{Eq. 2-4}$$

where C_k $(k = 1, \dots, p)$ is the *k*th connected region and $f(C_k)$ is the number of elements in region C_k. Next, all the other connected regions from the image are removed except for the region belonging to the candidate skull. However, some small holes still possibly exist in the candidate skull C_a as shown in Figure 2.3-c. To remove those small holes inside bone, the binary matrix is copied and inverted to form a new matrix, called the inverted matrix M (Eq. 2-5 and 2-6),

$$M = (M_{i,j}) \quad (i = 1, \dots, m\ and\ j = 1, \dots, n) \qquad \text{Eq. 2-5}$$

with

$$M_{ij} = \begin{cases} 1, & if\ I_{ij} \notin C_a \\ 0, & if\ I_{ij} \in C_a \end{cases} \qquad \text{Eq. 2-6}$$

where M_{ij} is the converted intensity of the pixel at the *i*th row and the *j*th column in the inverted matrix *M*. Using the connected component algorithm (CCA) again, q pieces

connected regions (D_1, D_2, ..., D_q) are obtained from the inverted matrix M. Using the identified regions of D_k (k = 1 to q), a series of new matrices is produced for each of the component of D_k. L_k ($k=1, 2, \dots, q$) is used to represent the pixels within the matrix for each component of D_k.

$$L_k = \left(L_{k\,i,j}\right), \quad (i = 1, \dots, m \text{ and } j = 1, \dots, n) \qquad \text{Eq. 2-7}$$

with

$$L_{k\,ij} = \begin{cases} 1, & if\ L_{k\,ij} \in D_k \\ 0, & if\ L_{k\,ij} \notin D_k \end{cases} \qquad \text{Eq. 2-8}$$

After finding each of the components which does not belong to the skull, the area of these components is computed. Using the computed areas, only those connected regions with an area less than a set threshold S is considered as a hole within the bone structure of the original scan. For this study based on the relative sizes of the objects found in brain CT scans, S has been set to 200 pixels which is a fair estimation of possible hole size. Once these holes have been identified inside the candidate skull structure, they are filled with bone intensity (equal to 1 in the binary matrix). This helps unify the overall identified bone structure by covering all the holes. A subset of the inverted matrices which are identified as holes within the bone structure is given as H_k ($k=1, 2, \dots, q$) to express the bone hole regions.

$$H_k = \begin{cases} L_k, & if\ \ f(D_k) \le S \\ O, & if\ \ f(D_k) > S \end{cases} \quad (k=1, 2, \dots, q) \qquad \text{Eq. 2-9}$$

where $f(D_k)$ is the number of elements in region D_k and O is a zero $m \times n$ matrix. Then, we can obtain the final detected skull Γ by combining the candidate skull matrix (J-M) with all whitened small holes matrices L_k as shown in Eq. 2-7, 2-8 and Figure 2.3-d.

$$\Gamma = (J - M) + \sum_{k=1}^{q} H_k \qquad \text{Eq. 2-10}$$

where M is the converted matrix defined in Eq-6, J is the matrix with every element equal to one. Thus, (J-M) represents the candidate skull corresponding to the connected region C_a.

2.2.2 Closed skull inspection

Followed by the skull detection, the second step in SSA algorithm is the closed skull inspection. This process aims to remove the slices with either unclosed skull or with the skull containing too many separated regions. The unclosed skull affects the following ideal midline identification since the symmetry value calculation through the exhaustive symmetric position search process is sensitive to the shape of the skull contour.

We define a new measure, called skull closing level F, using the number of zero matrices among all hole matrices H_k (k=1, 2, ..., q).

$$F = \sum_{k=1}^{q} g(H_k) \qquad \text{Eq. 2-11}$$

with

$$g(H_k) = \begin{cases} 1, & if\ H_k = O \\ 0, & \text{otherwise} \end{cases} \qquad \text{Eq. 2-12}$$

where H_k is the kth hole matrix which was defined in Eq. 2-9, O is a zero $m \times n$ matrix, and thus $g(H_k)$ is a binary state-variable used to express whether H_k is a zero matrix. When H_k is a zero matrix, it means that the kth connected-converted region D_k belongs neither to the candidate skull nor to the small bone hole. Therefore, those zero matrices

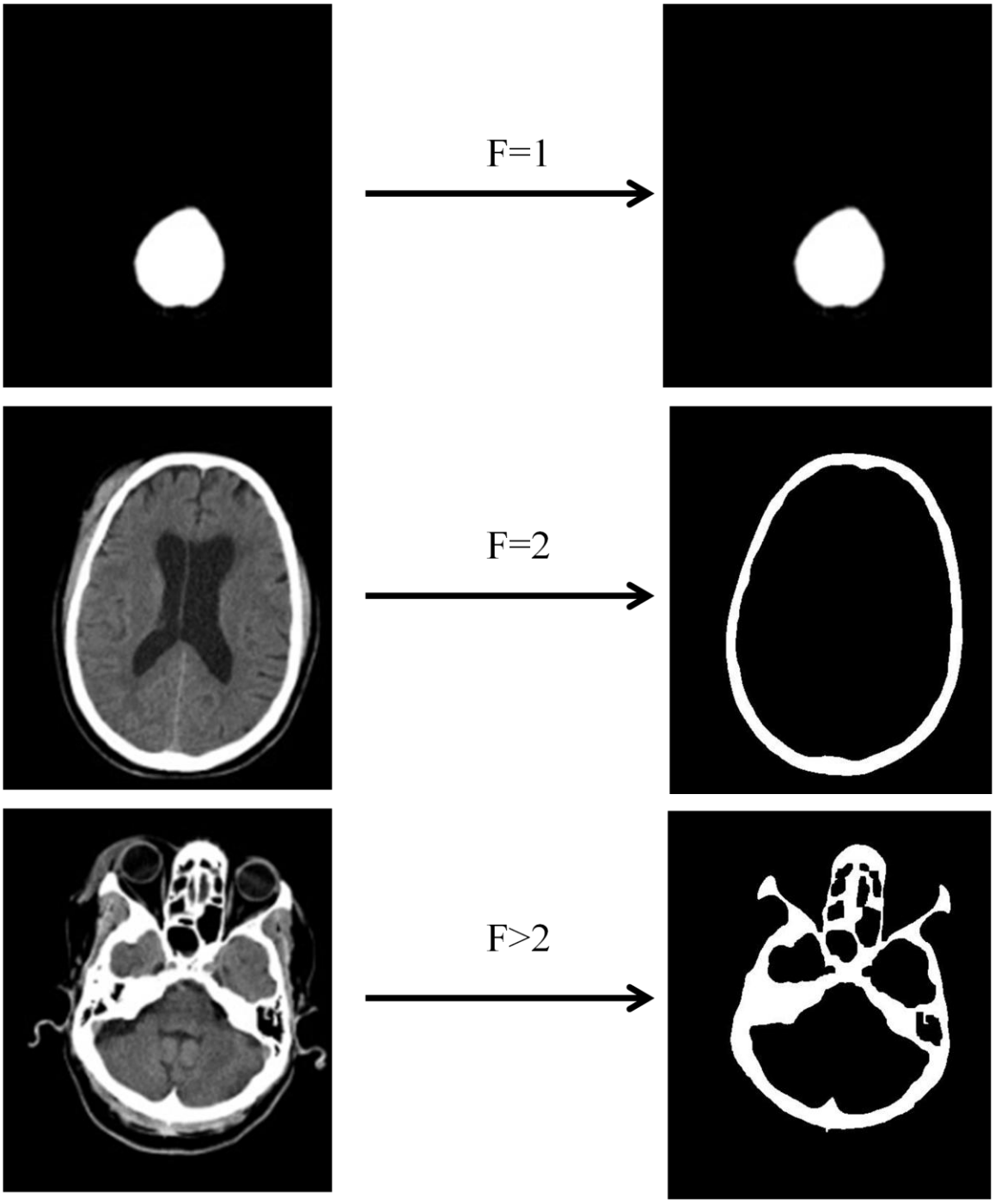

Figure 2.4 Closed skull inspection. The three left-side images are the raw CT images while the bottom three right-side images show the corresponding detected skulls. The black regions either inside or outside of the detected skull are the above mentioned H_k with zero matrix. Skull closing level of the three slices equals 1, 2, and more, respectively.

H_k should be the regions separated by the detected skull Γ as the black regions either inside or outside the detected skull shown in the three right-side figures of Figure 2.4.

If the computed skull closing level F is equal to 2, it implies that the skull is integrated and ideal for the following steps of detection, such as middle slice shown in Figure 2.4. If the computed skull closing level F equals to 1, it means the slice only shows a block of solid bone. As shown in the upper slice in Figure 2.4, this kind of slice is taken when the scan position close to calvaria. If the computed skull closing level F is larger than 2, as the bottom slice shown in Figure 2.4, the multiple closing region implies too much interference involved in the slice and therefore seriously affect the exhaustive symmetric position search in the following ideal midline detection. More, this kind of slices is usually taken when the scan position is far away from the center of ventricle. So the slices with F>2 are not appropriate for midline detection. Therefore, CT slices with F not equal to 2 cannot be used in midline detection due to an inappropriate scan position. The skull closing level measure can quantitatively evaluate the integrity of the skull in head CT images. After closed skull inspection, all images with $F \neq 2$ are removed from the slice subset.

2.2.3 Intracranial area detection

Based on clinical experience, the ideal CT slice for midline detection generally has larger intracranial area, such as the slices No. 22-30 in Figure 2.1. Hence in this step, the area of the inner region surrounded by the detected skull, namely the intracranial pixels, is calculated and sorted for all remaining slices in the subset.

In the subset of images acquired after the closed skull detection step, every CT image should contain only two black regions which are separated by the detected skull (F=2 in closed skull inspection). One of them is the intracranial region which contains the mass center of the skull and the other is the region outside of the skull. In order to calculate the intracranial area, the intracranial region has to be distinguished from region outside of the skull. This can be achieved using the coordinate of the skull's mass center.

Generally, the image moment m_{pq} of the order $p+q$ of the digital image Γ can be defined as below,

$$m_{pq} = \sum_{j=1}^{n} \sum_{i=1}^{m} i^p \cdot j^q \cdot \Gamma_{ij}, \quad (p = 0,1; q = 0,1) \qquad \text{Eq. 2-13}$$

where Γ_{ij} with the value of 1 or 0 is the intensity of the element at the ith row and jth column in the detected skull matrix Γ. Then, the coordinate of the mass center (x_0, y_0) of the detected skull can be obtained by

$$\begin{cases} x_0 = \frac{m_{10}}{m_{00}} \\ y_0 = \frac{m_{01}}{m_{00}} \end{cases} \qquad \text{Eq. 2-14}$$

Thus the connected-converted region D_{in} containing the coordinate of the skull mass center (x_0, y_0) is the intracranial region. The intracranial area S_{in} of this image is given by

$$S_{in} = f(D_{in}) \qquad \text{Eq. 2-15}$$

The intracranial area of every slice in the subset is calculated and sorted in descending order. The first λ slices with larger intracranial area are selected out for the following inspection. This number of λ is a variable that depends on the number of slices for one patient or physician's requirement.

$$\lambda = Min(\gamma, [\eta * \Phi]) \qquad \text{Eq. 2-16}$$

where γ is a default number of selected slices and η is the selected percentage of the whole number of slices Φ. After experimenting with various values, $\gamma = 8$ and $\eta = 20\%$ were finally chosen for this study.

2.2.4 Convexity inspection

According to practical experience, another important characteristic of an ideal head CT image for midline detection is generally a good convexity for the intracranial region. For instance, the intracranial regions of the slices No.19-20 in Figure 2.1 which are not ideal for midline detection both have integrated skull and larger intracranial area but show partially concavity. In contrast, intracranial regions of slices 26 through 28 have good convexity. In addition, the concave shape of the intracranial region could affect the accuracy of the exhaustive symmetric position search, which is performed in the subsequent midline detection.

To quantitatively measure and evaluate the convexity of the intracranial region, we define a new measure Λ, called the intracranial convex measure. As shown in Figure 2.5-c, we extract the contour of the intracranial region. Then we can scan those pixels row by row. We define the far left and far right junctions (the blue points) of the *i*th row line (the upper red dash line) and the intracranial contour (the black curve) as points LP_i and RP_i in Figure 2.5-c. We use the function $\xi(i,j)$ to describe the out-of-intracranial-region pixels between LP_i and RP_i on the *i*th row as the green bold line shown in Figure 2.5-c.

$$\xi(i,j) = \begin{cases} 1, & (i,j) \notin R \text{ and } LP_i<j<RP_i \\ 0, & \text{otherwise} \end{cases} \qquad \text{Eq. 2-17}$$

where R represents the intracranial region. Then the number of the out-of-intracranial-region pixels on the ith row $\Psi(i)$ is given as below

$$\Psi(i) = \begin{cases} \sum_{j=LP_i}^{RP_i} \xi(i,j), & \text{if } \exists\ LP_i \text{ and } RP_i \\ 0, & \text{otherwise} \end{cases} \qquad \text{Eq. 2-18}$$

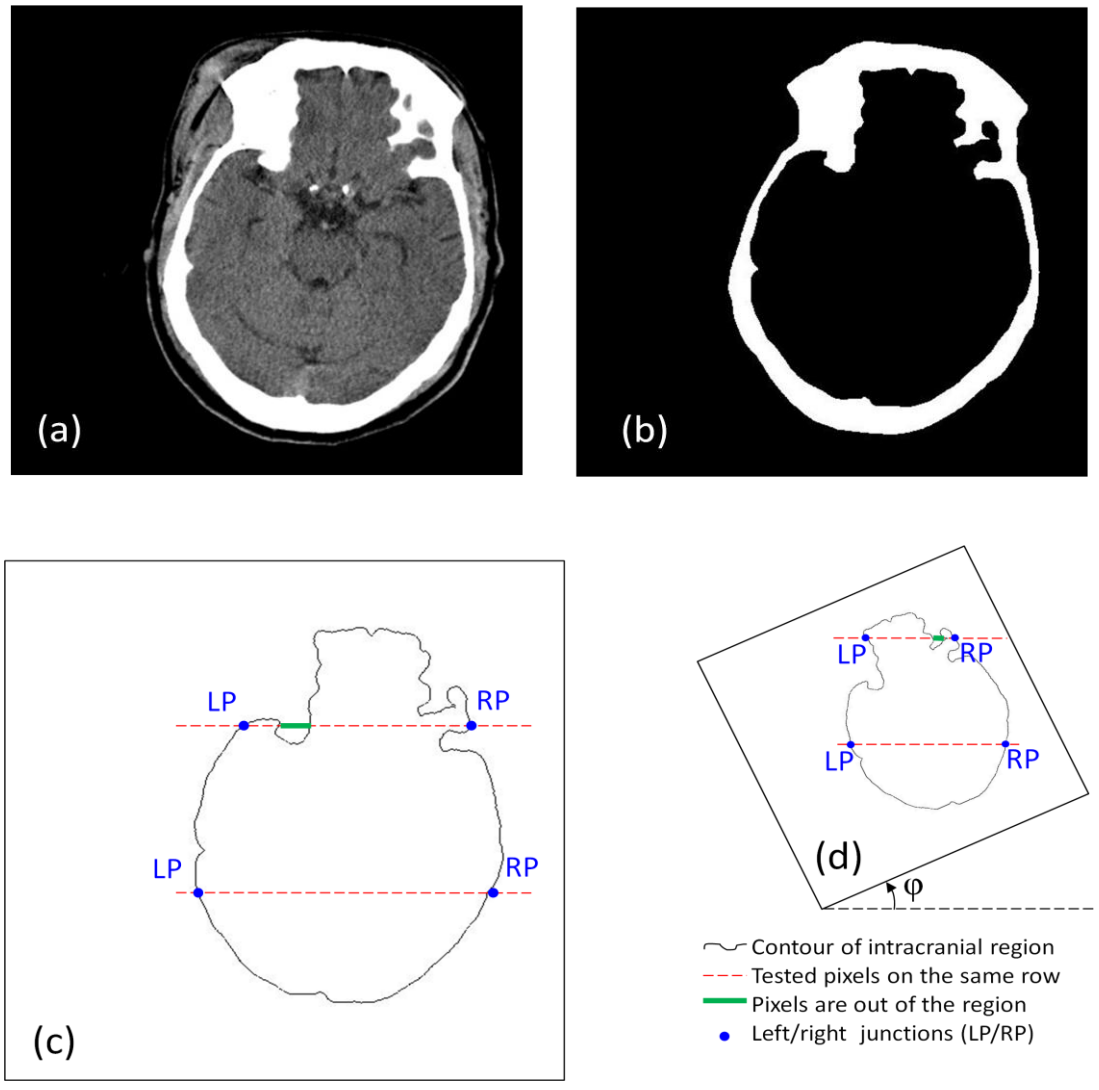

Figure 2.5 Convexity inspection on a CT slice (a) the raw slice, (b) the detected skull, (c) the calculation of the intracranial convex measure using the intracranial contour, (d) the intracranial convex measure calculation on the image rotated by angle φ.

We define the intracranial convex measure Λ using the total number of the out-of-intracranial-region pixels on all *m* rows of the image.

$$\Lambda = \sum_{i=1}^{m} \Psi(i) \qquad \text{Eq. 2-19}$$

Then, we can rotate the image by φ degree as shown in Figure 2.5-d. The intracranial convex measure at angle φ can be calculated and noted as Λ_{φ}.

$$\Lambda_{\varphi} = \sum_{i=1}^{m} \Psi_{\varphi}(i) \qquad \text{Eq. 2-20}$$

where $\Psi_{\varphi}(i)$ the number of the out-of-intracranial-region pixels on the *i*th row in the image rotated by angle φ. With the sum of the all Λ_{φ} at all rotating angles, the total intracranial convex measure Λ_{Total} is given as below

$$\Lambda_{Total} = \sum_{\varphi=1^{\circ}}^{180^{\circ}} \Lambda_{\varphi} = \sum_{\varphi=1^{\circ}}^{180^{\circ}} \sum_{i=1}^{m} \Psi_{\varphi}(i) \qquad \text{Eq. 2-21}$$

Larger values of the total intracranial convex measure Λ_{Total} represent increasingly worse convexity of the intracranial region in a CT image. Using the sorted Λ_{Total}, we can keep the better λ CT slices in the slice-subset by removing the ones with worse convexity. Value of λ can be decided by Eq. 2-16. For the example under study, using $\gamma = 6$ and $\eta = 15\%$ around 6 slices were obtained for the slice subset after convexity inspection.

2.2.5 Ventricle visibility inspection

In clinical practice, physicians usually use ventricular system to estimate the actual midline towards diagnosing the midline shift. Thus the visibility of ventricles is vital in

the actual midline detection. In the last step of SSA algorithm, the selection focuses on the visibility of the ventricles in the intracranial region.

Figure 2.6 shows the schematic diagram of the ventricle visibility inspection step in SSA algorithm. After the first four steps of SSA algorithm, the skull is extracted in the CT slice. In this step, the main purpose is to select a few slices with the clearest ventricles inside the intracranial region.

K-means clustering is used to distinguish ventricles from other tissue/interference in the image. First, we assume that four kinds of objects of interest, namely bone/blood, light matter, grey matter, and ventricular tissue exist in the intracranial region of the image.

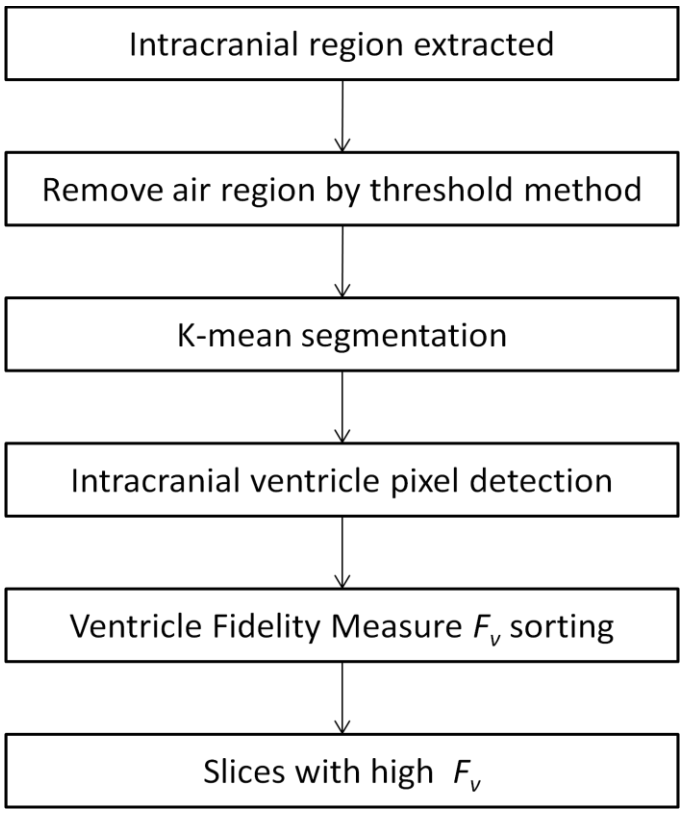

Figure 2.6 Schematic diagram of the ventricle visibility inspection

In addition, in some cases, air may exist inside the intracranial region (See figure 2.7). We should carefully inspect for air and remove the interference of air in the following detection. The intracranial air is never normally present in this location as shown in Figure 2.7. Air bubbles may be millimeters in size, or large collections of air may be seen. Air can also leak intracranially from a mastoid and associated temporal bone fracture [85]. Postoperative gas can be a normal finding in patients after craniotomy and may persist for weeks [86]. Rearly, air can be introduced latrogenically through venous and arterial catheters [87]. Intracranial gas can also occur in dive-related decompression illness [10]. Intracranial air appears black on all CT images. For instance, the intracranial air in Figure 2.7 is the black region close to the calvaria. To remove this region, we use threshold method by removing the intracranial pixels with the intensity in the range of 0-5.

Figure 2.7 Brain CT image with air in intracranial region

Except for the possible existing intracranial air, there are four objects of interest considered inside the intracranial region. Each of the four objects has a particular range of gray scale. Using K-means clustering, the pixels related to lowest intensity center are labeled as belonging to the ventricle class.

Here, a new measure, called Ventricle Fidelity Measure (F_v), is introduced to describe the visibility of the ventricles in CT slices. Ventricle Fidelity Measure is defined by dividing the number of pixels labeled as the ventricle class by the total number of pixels after the k-means clustering. Generally, the larger Ventricle Fidelity Measure is, the more visible the ventricle is in image. Using a threshold (120 pixels in this work), only those CT slices with large F_v are kept in the SSA subset for the subsequent midline detection. It is worth noting that Ventricle Fidelity Measure only estimates the quality of CT slice containing ventricle. There is also a chance that some slices might be selected mistakenly due to the inherent noise within the scan or improper intensity center chosen by the k-means method for the ventricle clusters. However, given the fact that usually numerous candidate CT slices get shortlisted at this step, the chances of selecting valuable CT slices within this subset is high. In sum, finding the CT slices containing clear ventricles (large F_v) is a key point for the slice selection step based on k-means clustering and F_v sorting in the SSA algorithm.

Using the sorted $F_{v,}$ we can keep the better λ CT slices in the slice-subset by removing the ones with worse Ventricle Fidelity. Value of λ can be decided by Eq. 2-16. In this study, using $\gamma = 4$ and $\eta = 10\%$, around 4 slices were obtained finally in the SSA subset.

2.3 Result and discussion

2.3.1. Data

This database contains 3133 axial CT scan slices acquired across 70 patients with cases of both mild and severe Traumatic Brain Injuries (TBI). All the available CT scans have been utilized in testing the system's processes and in the estimation of ideal midline.

2.3.2. Results and discussion

With the implementation of the SSA algorithm on the raw slices, only a few slices which are appropriate for midline detection remain in the SSA subset. For instance, the number of initial CT slices for the subject used for the results presented in Figure 2.8 was 40. Most of these 40 slices are not suitable for midline detection, as some slices contain too much noise and interference from other organs/tissues, some other slices have small representation of intracranial area, some slices show unclosed skull, and some slices contain too little ventricle representation for detection.

In the first step of the SSA algorithm (See the diagram in Figure 2.2), the skull on every slice is detected. Closed skull inspection remove all slices with $F \neq 2$. Figure 2.9 shows that 15 slices remain after the closed skull inspection. Compared with all raw slices of this patient in Figure 2.8, those first several slices in the raw slice set with much interference from other organs are removed from the list.

With the implementation of the third step in SSA, intracranial area detection, the slices with smaller intracranial area are removed from the subset. Figure 2.10 shows the result of applying the intracranial area detection. Compared with the images in Figure 2.9, the

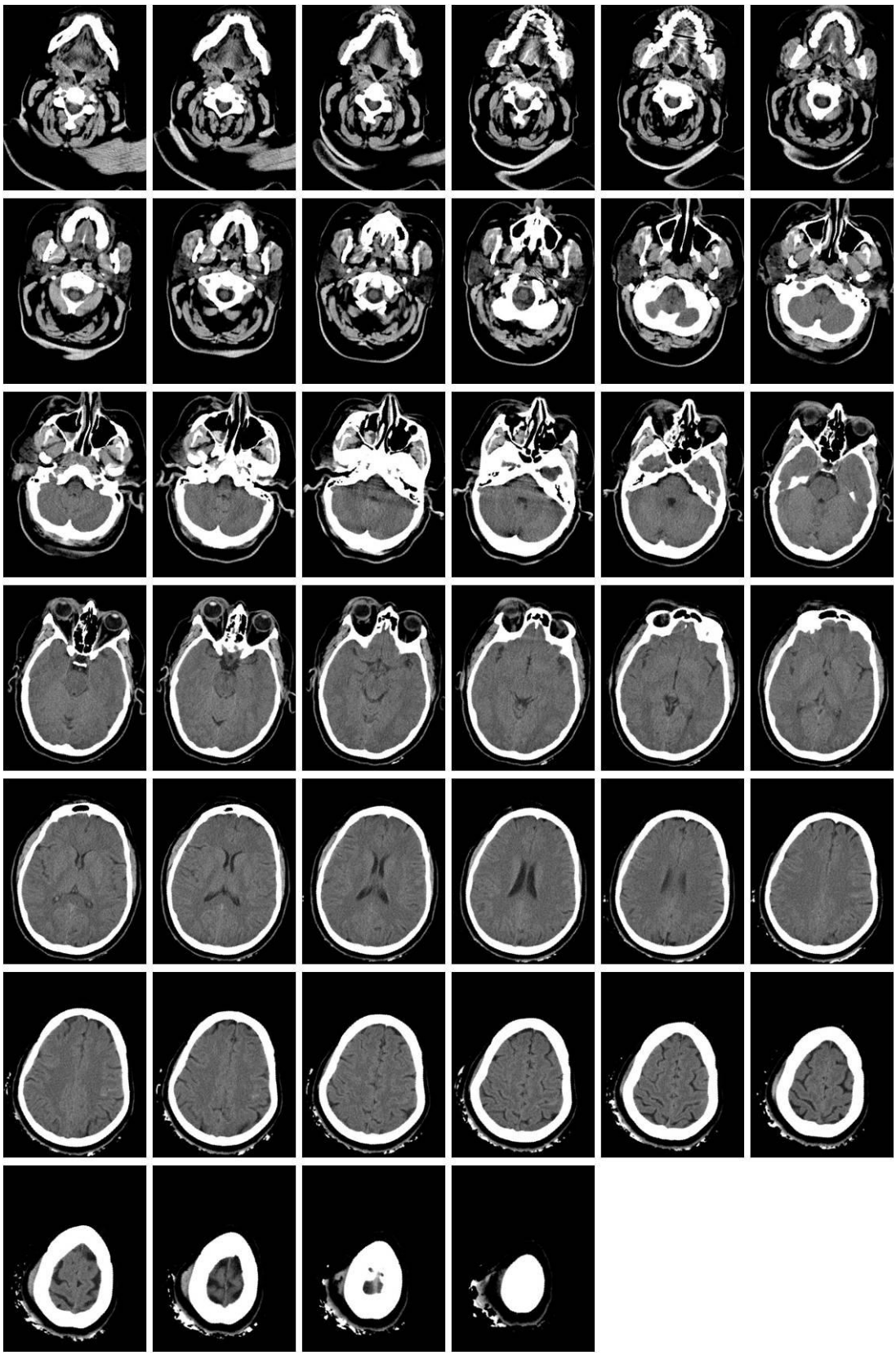

Figure 2.8 Raw CT slices (40 slices) from one patient's head CT scan.

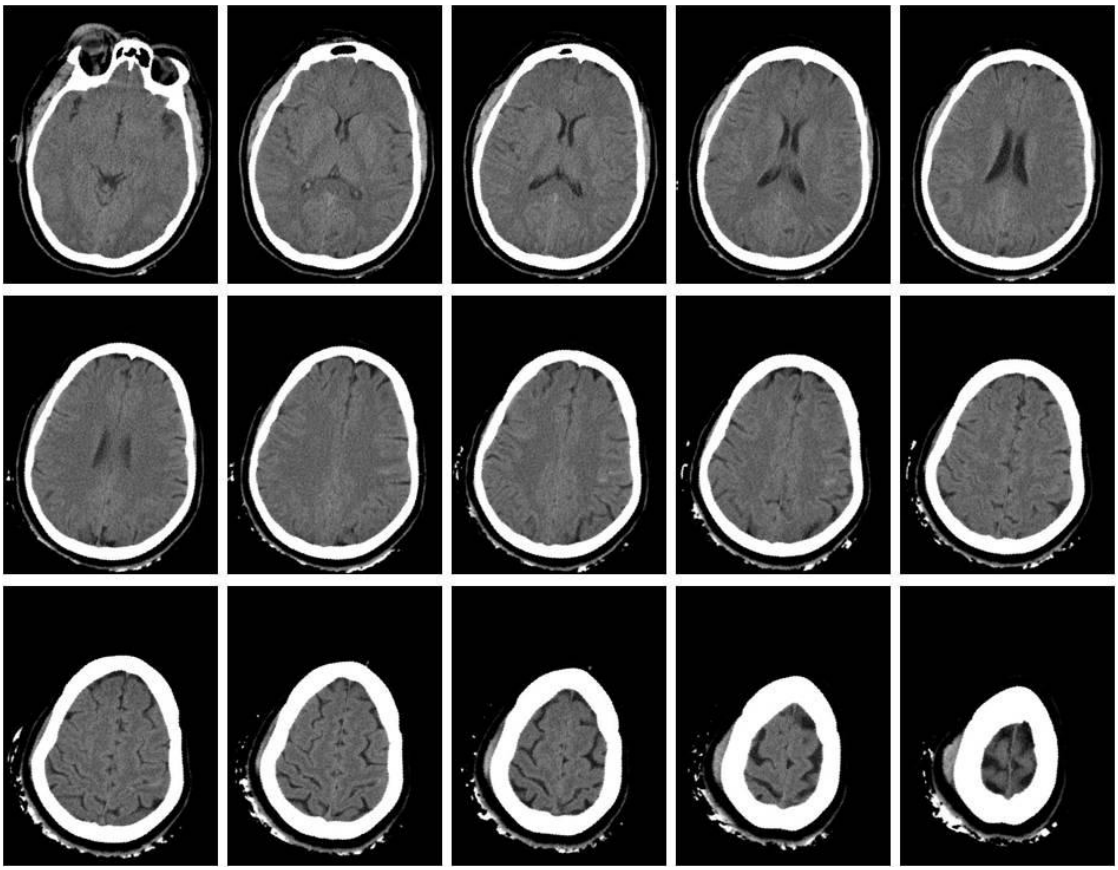

Figure 2.9 Selected CT slices after the closed skull inspection

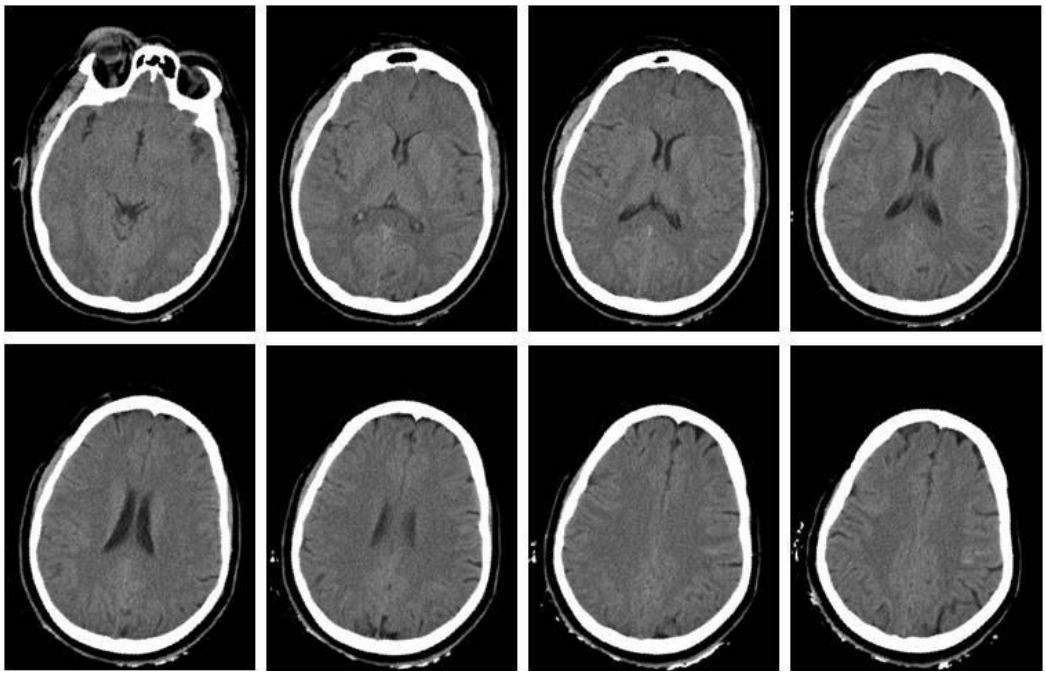

Figure 2.10 Selected CT slices after the intracranial area detection

slices removed in this step not only have small intracranial area but also contain little to no ventricle in them. Thus, those removed slices are indeed not suitable for midline detection.

The fourth step in SSA is convexity inspection. Six slices remains after the convexity inspection as shown in Figure 2.11. All the skulls of these six slices have good convexity and are appropriate for the exhaustive symmetric position search in ideal midline detection. Among them, the slices with clear ventricle information are selected out using the followed ventricle visibility inspection.

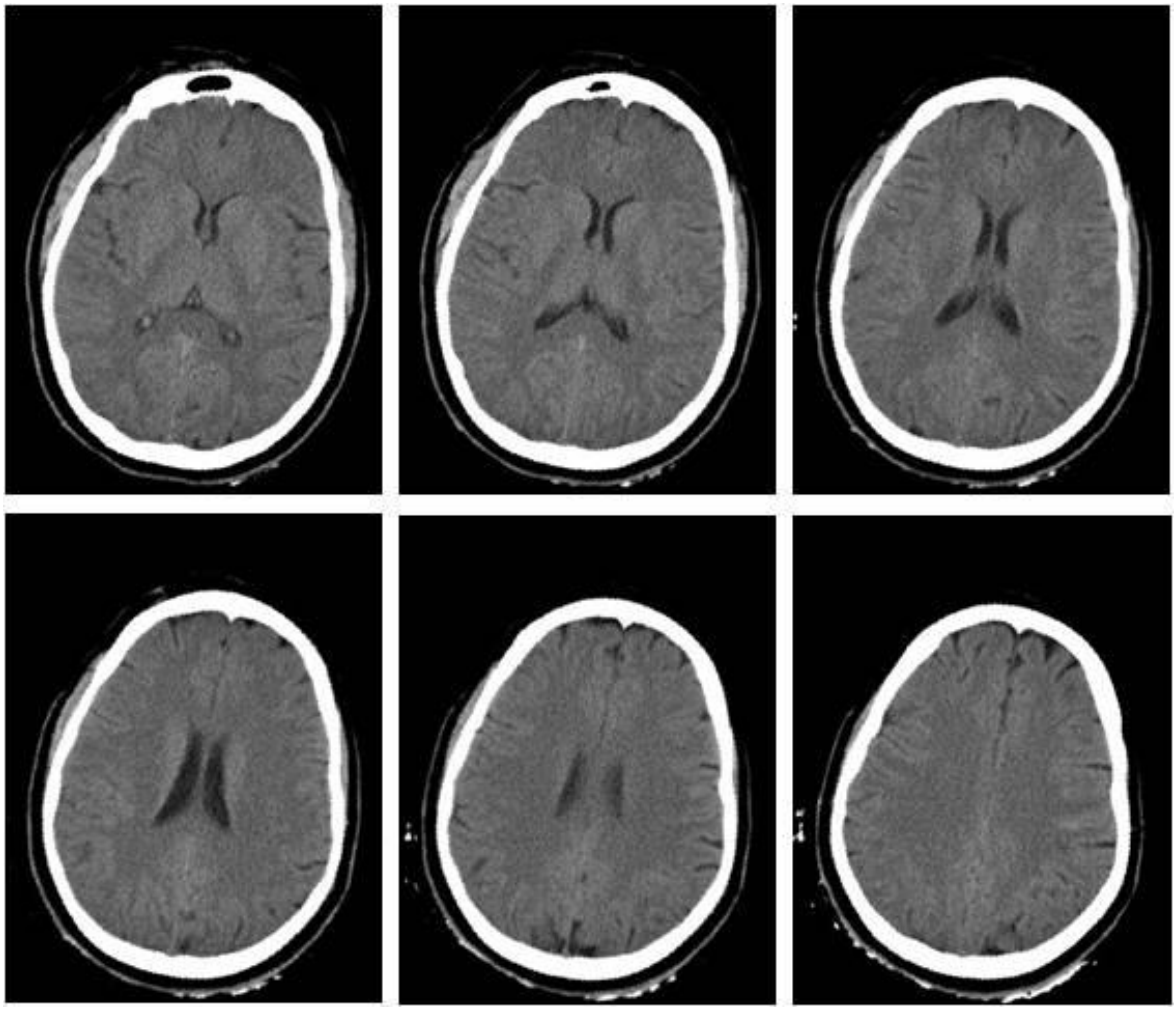

Figure 2.11 Selected CT slices after the convexity inspection

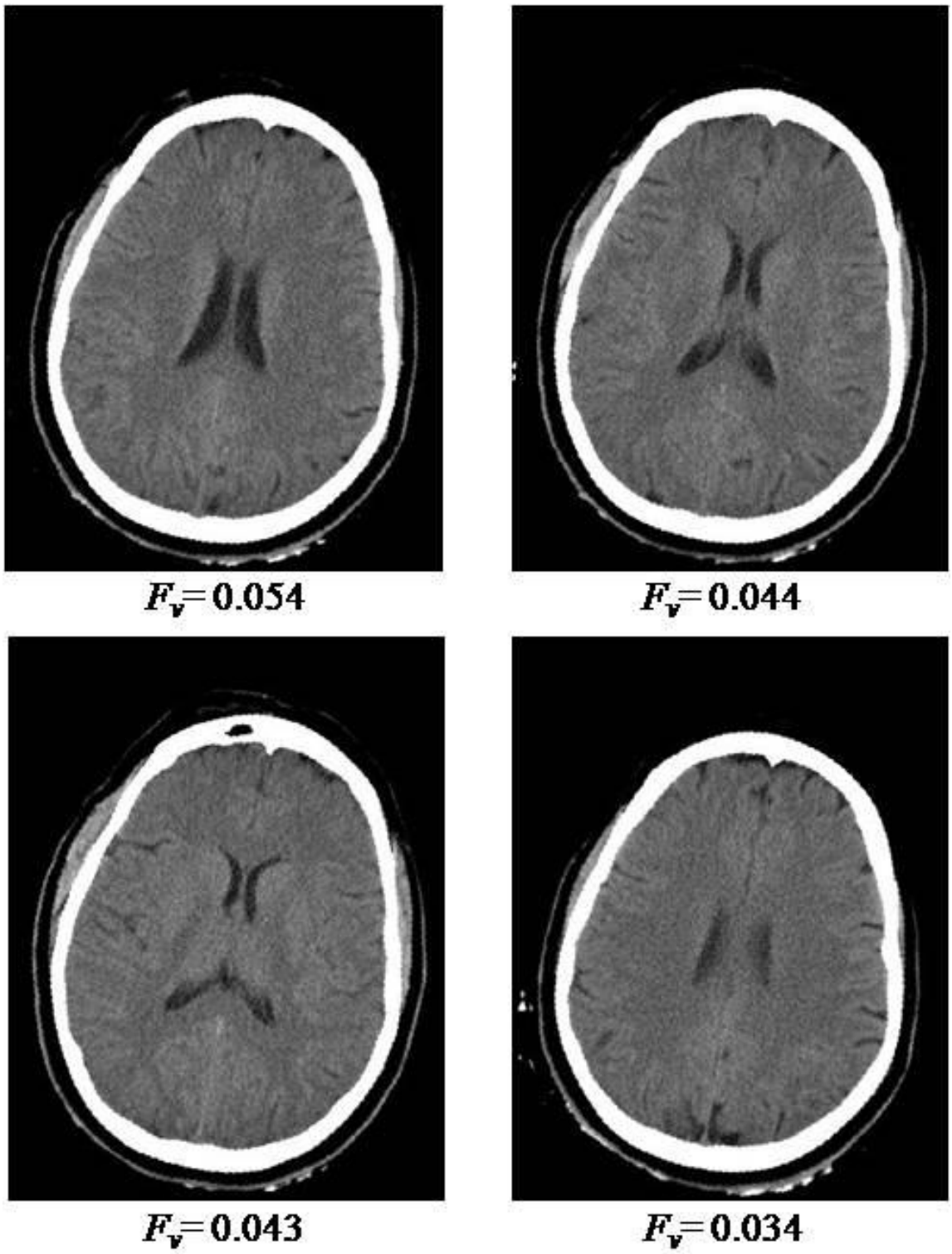

Figure 2.12 CT slices after F_v sorting in Ventricle visibility inspection

In the ventricle visibility inspection step, with the k-mean segmentation, the pixels belonging to ventricle class are used in the calculation of ventricle fidelity measure (F_v). The larger the ventricle fidelity measure is, the more ventricle information the slice would show. As shown in Figure 2.12, the slices are sorted by the value of F_v. Four slices with large F_v value are selected as the candidate slices in the SSA subset for the following midline detection. It can be seen that the top left slice with the largest ventricle fidelity measure F_v= 0.054 shows the largest ventricles. This slice is considered as the first candidate slice in the SSA subset.

2.4 Summary

The CT slice selection algorithm is primarily based on the anatomical characteristics of the skull and closely simulates the process of manual CT slice selection and decision making in midline estimation by physicians in clinical practice. With the implementation of SSA, a vast reduction can be achieved of the number of slices that is used for the computation of IML detection steps. For instance, the case used in Figure 2.8-2.12, the slices selected by the SSA algorithm is 4 pieces which is much less than the 40 pieces raw slices of this patient. Those selected slices with closed skull, large intracranial area, good convexity, and clear ventricle information have been found to be acceptable for use in midline detection with the physician's confirming. Having fewer and more appropriate slices effectively increases the efficiency of the algorithm and also has the potential to save the cost and time required in practice.

Chapter 3 Ideal Midline Detection

3.1 Background and introduction

Human brain has two hemispheres with an approximate bilateral symmetry distinguished by ideal midline (IML), which is the longitudinal fissure marked by the falx cerebri in the mid-sagittal plane [10, 88]. The computer-aided estimation of IML has attracted a great deal of attention in the recent two decades [88-90]. The inter-hemispheric fissure line segments have been widely used to detect the ideal midline on MRI images which usually has a high visibility on the fissure line [91, 92]. In the case of brain CT slices, longitudinal fissure cannot be used as an only primary index for detection due to the low-to-zero visibility of the fissure which can seriously affects the accuracy of detecting the Mid-Sagittal Plane (MSP) or IML. Moreover, some pathological symptoms, such as a tumor, may curve the fissure and completely change the direction of the fissure. To avoid the above limitation, skull symmetry has been included as another important anatomical feature in MSP/IML detection [83, 92]. G. Ruppert *et al.* extracted the MSP based on bilateral symmetry maximization [92]. W. Chen *et al.* combined bone symmetry and direct detection of the anatomical features in CT images in IML detection [9]. This method works effectively and accurately on a single CT slice but lacks connection or comparison with the detection results from other CT slices of the same patient.

In this chapter, we propose a four-step algorithm to automatically detect brain ideal midline on CT images by considering both anatomical features and the connections among CT slices.

3.2 Methodology

After the slice selection is performed using CT Slice Selection Algorithm (SSA) proposed in Chapter 2, only a few (around 4 pieces) appropriate slices are considered in ideal midline detection. Ideal midline detection (IML detection) is designed as a two-step procedure, an approximate IML detection and a refined IML detection, with the full considerations of both anatomical features and the connections among CT slices.

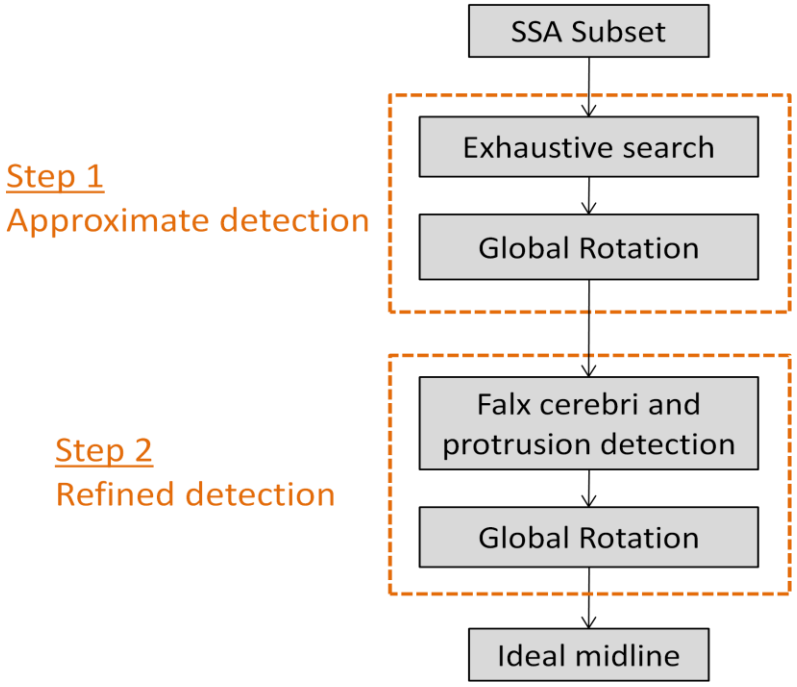

Figure 3.1 Schematic diagram of ideal midline detection

As the schematic diagram shown in Figure 3.1, in the first step, the ideal midline can be approximated using an exhaustive symmetric position search based on the skull symmetry. More, including other features of the skull and brain can help improve the accuracy of the approximation. Thus, in the refined IML detection step, the bone

protrusion on the upper part of the skull and the falx cerebri in the lower part are used to accurately detect the position of the ideal midline. To fully consider the connection among the slices in the subset, we utilize a global rotation assumption in both steps to determine the rotation angle of the skull. This method can further reduce the detection error due to individual non-ideal image.

3.2.1 Approximate IML detection

To find the approximate ideal midline on a brain CT image, we use the exhaustive symmetric position search algorithm which was a continuation of the work done by Wenan Chen *et. al.* on ideal midline detection [9]. To improve the accuracy of the algorithm, a few modifications are made in the exhaustive search and a global rotation method is firstly used in the approximate ideal midline detection.

We use an exhaustive rotation angle search around the mass center of the skull to find an line which can maximize the symmetry of the resulting halves. In Chapter 2, the skull Γ and its mass center (x_0, y_0) have been determined by Eq. 2-10 and Eq. 2-14, respectively. As shown in Figure 3.2, the row symmetry is defined as the difference in distance between each side of the skull edge and the current approximate midline. The CT image is rotated around the mass center of the skull. The symmetry cost S_θ of the image at the rotation angle θ is calculated as the sum of all row symmetry in the resulting image as shown in Eq. 3-1.

$$S_\theta = \sum_{i=1}^{m} |l_i - r_i| \qquad \text{Eq. 3-1}$$

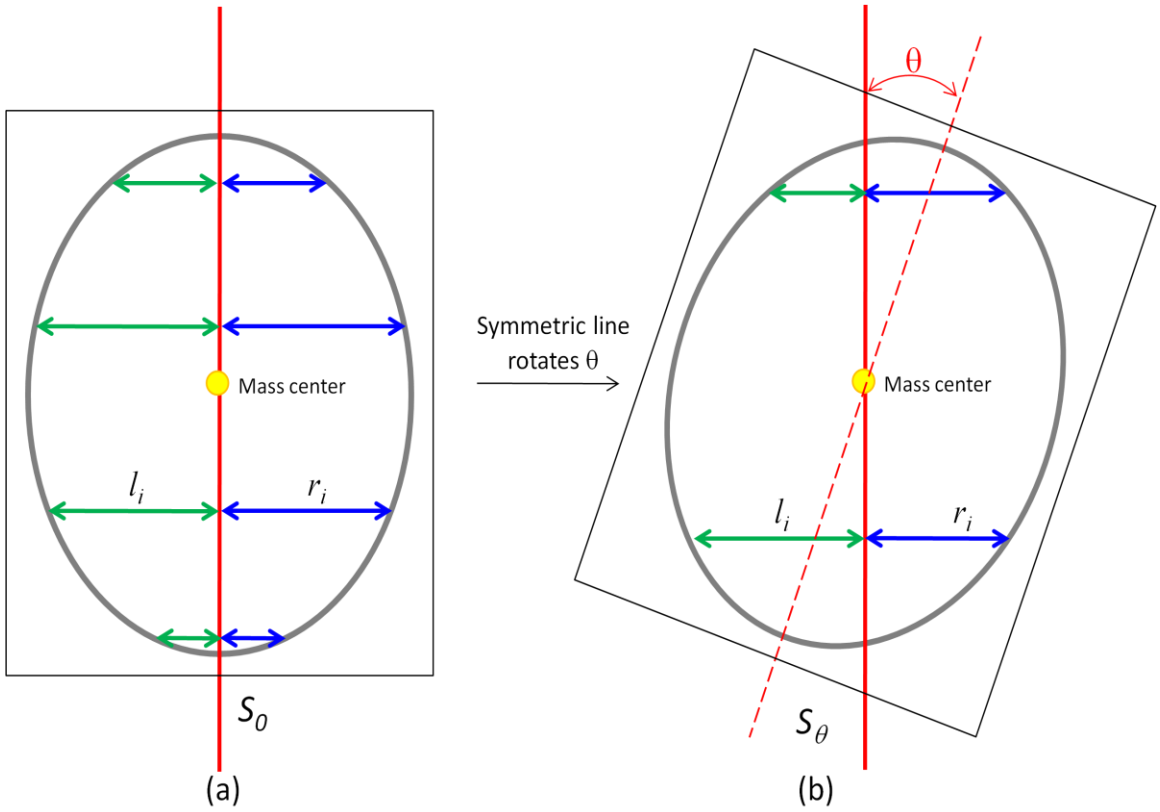

Figure 3.2 Symmetry cost calculation. The symmetric line passes through the mass center. Measure l_i and r_i are the distance between the edge of the skull on the left/right side and the current approximate midline at the *i*th row. (a) the slice with 0 rotation angle, (b) the slice with θ rotation angle.

where m is the number of rows in the image with the rotation angle θ ($-45° \leq \theta \leq +45°$ as used in this study) and measure l_i and r_i are the distance between the edge of the skull on the left/right side and the current approximate midline at the *i*th row. More details can be found in [9]. Finally, the rotation angle θ with the minimum symmetry cost S_θ determines the rotation direction of the midline of the brain for each particular CT slice.

$$\theta_p = \arg\min_{\theta_{pj}}[S_{\theta_{p1}}, S_{\theta_{p2}}, \cdots S_{\theta_{pl}}] \qquad \text{Eq. 3-2}$$

where θ_p is the rotation angle of the midline on the p*th* slice and $S_{\theta_{pj}}$ is the symmetry cost of the p*th* slice at the rotation angle θ_{pj}.

All CT slices in the SSA subset are processed one piece at a time using exhaustive symmetric position search. However, due to the non-uniform-thickness of the skull or due to serious deformation of the skull on one side after injury, it is hard to get an accurate position of the midline by processing only one slice. In this work, a global rotation assumption is used to decide the approximate ideal midline of all the CT images from one patient with full consideration of the connection among all the slices.

In the global rotation assumption, we assume that all CT images of one patient have the same rotation angle of the ideal midline due to the fixed posture of the patient during scanning. The rotation direction of the approximate ideal midline is determined by the median value of the rotation angles of all 6 slices in the SSA subset as shown below.

$$\theta_a = \underset{\theta_p}{median}[\,\theta_1, \theta_2, \cdots \theta_\lambda\,] \qquad \text{Eq. 3-3}$$

where the angles $\theta_1, \theta_2, \cdots \theta_\lambda$ are the rotation angles of the midlines determined by the exhaustive symmetric position search, λ is the number of slices in the SSA subset, and θ_a is the approximate ideal midline of the whole set of slices. At the end of the approximate IML detection, the approximate ideal midline on each slice is calibrated to the vertical direction by rotating the skull by $-\theta_a$ angle.

3.2.2 Refined ideal midline detection

Once the approximate midline is estimated and calibrated, brain anatomical features, such as the position of the falx cerebri and protrusion of skull bone, are used to refine the detection. In the detection of the falx cerebri and protrusion, we use the same algorithm from our previous work [9].

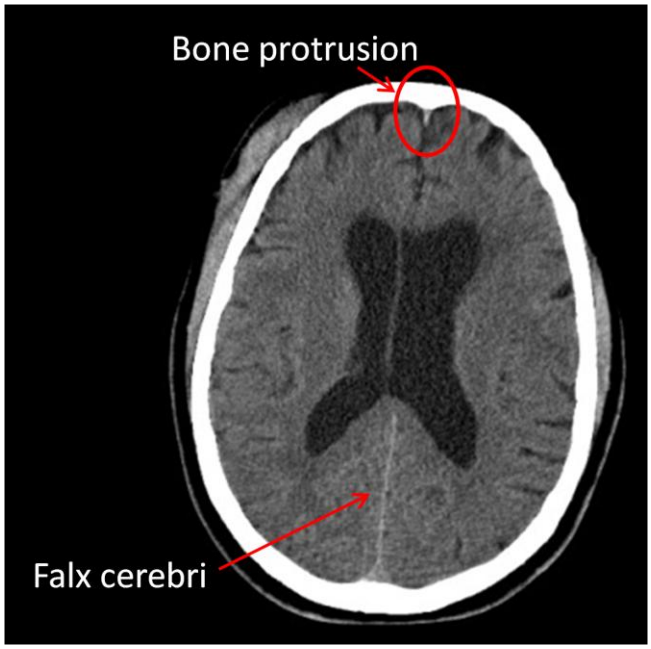

Figure 3.3 The falx cerebri and the bone protrusion

The falx cerebri is a strong arched fold of dura mater that descends vertically in the longitudinal fissure between the left and right cerebral hemispheres (Figure 3.3). In this work, edge detection method and Hough transform are used to detect this anatomical feature quickly and accurately. On the other hand, a bone protrusion is located in the anterior section of the skull. As shown in Figure 3.3, the bone protrusion curves down to a minimum point which is considered to be the upper starting point of the falx cerebri. To locate the lowest point of the protrusion curve, the derivative of the curve is calculated in a limited neighborhood area, which has been chosen to be 10-15 pixels in this work. The local minima point *a* is determined by the following equation.

$$x_a = \arg\max_x [\Re(x+w) + \Re(x-w) - 2\cdot\Re(x)] \qquad \text{Eq. 3-4}$$

where the function $\Re(x)$ is the extracted curve of the interior bone edge and w is the neighborhood width. In fact, several small local minimal points may exist around the neighbor area of the protrusion due to the noise of the image or the irregularities of the skull. Using the maximal second derivative of the curve as the point a, Eq. 3-4 is used to successfully extract the true protrusion minimal point by avoiding the influence of noise. More details of the detection of the falx cerebri and the bone protrusion can be found in [9].

Using the detected falx cerebri and the bone protrusion, we can obtain the refined rotation angle θ_q of the midline on each slice. Again, the global rotation assumption is used to determine the refined ideal midline of the whole set of slices. Rather than using the median method in the approximate midline detection, the weighted average method is used in this refine detection step. The rotation angle θ_f of the refined ideal midline of all the slices is given by

$$\theta_f = \frac{\sum_{q=1}^{\lambda} \mu_q \cdot \theta_q}{\sum_{q=1}^{\lambda} \mu_q} \qquad \text{Eq. 3-5}$$

where θ_q is the refined rotation angle of the midline on the qth slice and μ_q is the weight of θ_q in the refined IML detection calculation.

$$\mu_q = \begin{cases} 1 & \text{if the falx cerebri and protrusion are both detected} \\ \nu_1 & \text{if only the falx cerebri is detected} \\ \nu_2 & \text{if only the protrusion is detected} \\ 0 & \text{if neighter falx cerebri nor protrusion is detected} \end{cases} \qquad \text{Eq. 3-6}$$

where the values of ν_1 and ν_2 are both in the range of 0-1. We set $\nu_1 = 0.2$ and $\nu_2 = 0.3$ in this work.

At the end of the refined IML detection, the ideal midline on each slice is calibrated again to the vertical direction by rotating the skull by $-\theta_f$ angle. Therefore, in the two-step ideal midline detection, the ideal midline is centered by the mass center of the skull and rotated by an angle of $-(\theta_a + \theta_f)$ from the original position in the slice.

3.3 Results and discussion

3.3.1 Data

This database contains original 3133 axial CT scan slices acquired across 70 patients with cases of both mild and severe Traumatic Brain Injuries (TBI). All the available 280 CT images in the SSA subset have been utilized in testing the ideal midline estimation of the proposed system.

3.3.2 Results and discussion

The result of the ideal midline detection is displayed in Figure 3.4. With the implementation of the algorithm, we can see that the detected ideal midline is accurately located in the middle of the skull and that the skulls in each scan are calibrated correctly.

In order to quantitatively measure the performance of the proposed system, the collaborating physician manually estimated IML is used as the ground truth. With a strict definition of accuracy, which is an allowed error of three pixels in horizontal distance δ between the estimated IML and the ground truth, the accuracy of IML estimation in this system is calculated as below.

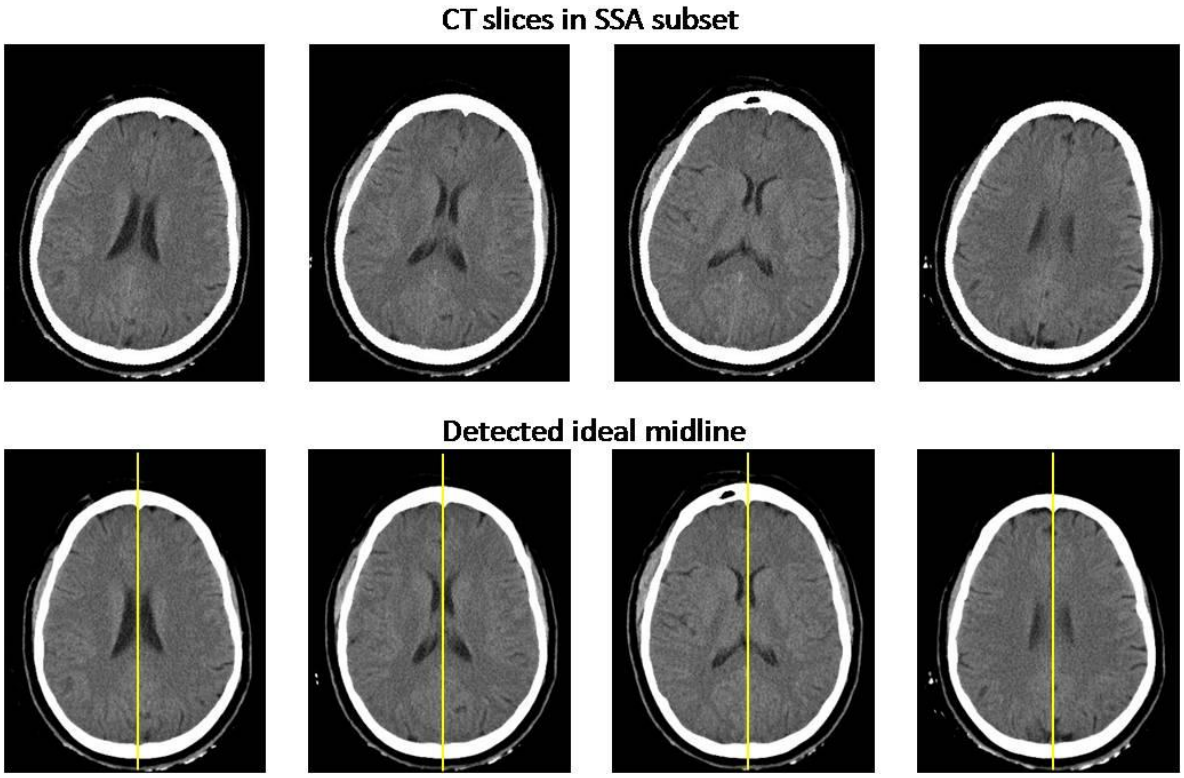

Figure 3.4 The results of the ideal midline detection. Upper figures are the raw slices selected by SSA algorithm, while the bottom figures show the corresponding detected ideal midline

As Figure 3.5 shows, two possible spatial relationships between the ground truth ideal midline (red dash line) and the detected one (blue solid line) can be used for calculation of the difference between the two methods. In case 1 (Figure 3.5-a), there is no cross between the ground truth ideal midline (red dash line) and the detected line (blue solid line). In case 2 (Figure 3.5-b), the point of crossing makes the two lines build two triangles. The values d_1 and d_2 represent the distance between the top row points distance and bottom row points distance of the two lines. The value h_0 is the length of the ground truth ideal midline between the top and bottom rows in case 1, while h_1 and h_2 are the

length of two segments of the ground truth line separated by the point of crossing, respectively. The horizontal distance δ between the ground truth midline and the detected one is calculated as follows:

$$\delta = \frac{S}{h} \qquad \text{Eq. 3-7}$$

where S is the area enclosed by the two line segments and the top and bottom line, while h is the length of the ground truth. Thus, $h=h_0$ in case 1 and $h=h_1+h_2$ in case 2.

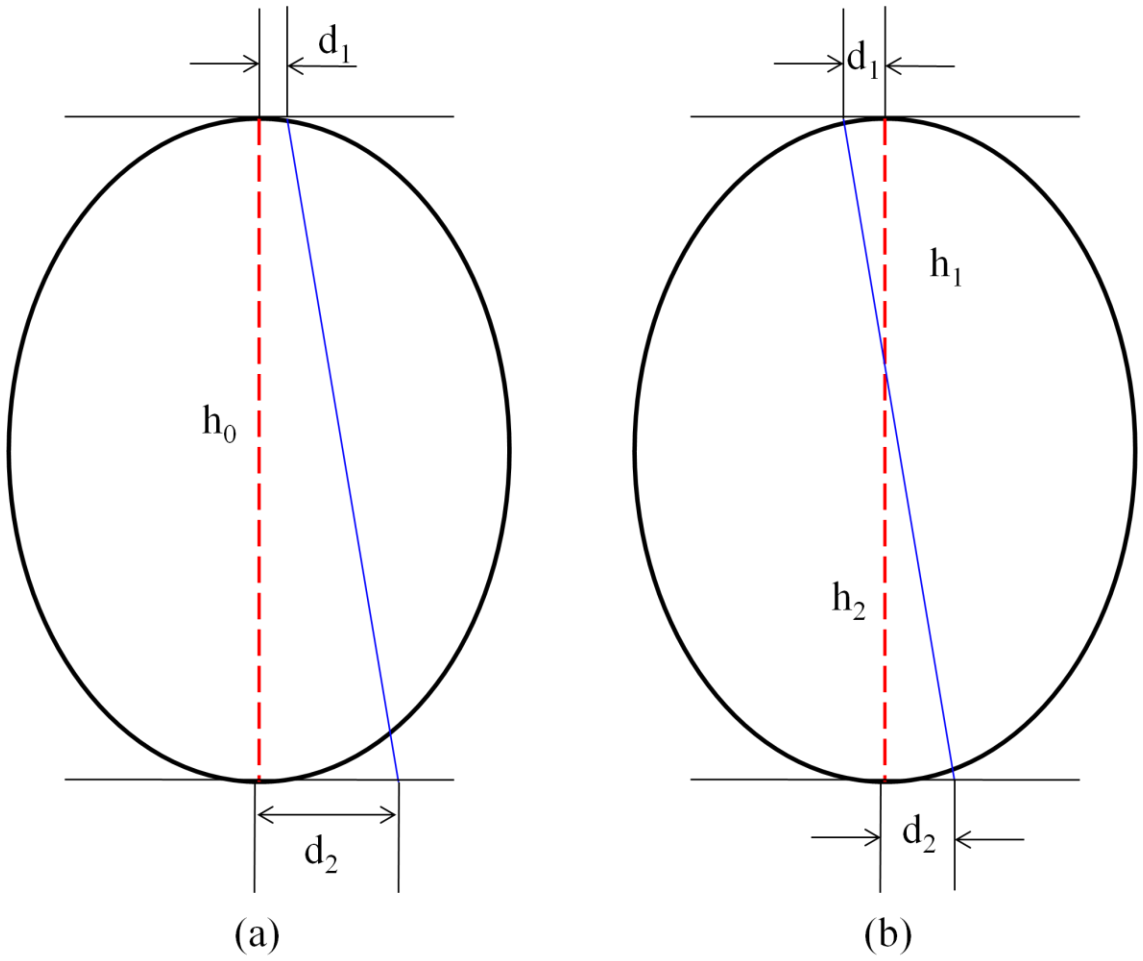

Figure 3.5 Two possible cases of the relationship between the ground truth ideal midline (red dash line) and the detected ideal minline (blue solid line).

In case 1,

$$S_{case\ 1} = \frac{1}{2}(d_1 + d_2)h_0 \quad \text{Eq. 3-8}$$

$$\delta_{case\ 1} = \frac{d_1+d_2}{2} \quad \text{Eq. 3-9}$$

In case 2,

$$S_{case\ 2} = \left(\frac{1}{2}d_1h_1 + \frac{1}{2}d_2h_2\right) \quad \text{Eq. 3-10}$$

$$\frac{d_1}{d_2} = \frac{h_1}{h_2} \quad \text{Eq. 3-11}$$

Then, the horizontal distance δ in case 2 can be calculated as:

$$\delta_{case\ 2} = \frac{d_1^2+d_2^2}{2(d_1+d_2)} \quad \text{Eq. 3-12}$$

Table 3.1 Comparison on the accuracy of IML estimation

Method	Our method	Method in [9]
Number of patients	70	40
Number of CT slices	280	391
Image format	JPEG	JPEG
Image resolution	512 ×512	512 ×512
Criterion for accuracy	$\delta \leq 3$	$\delta \leq 3$
Accuracy	96.9%	95%
Mean value of error δ	2.1	2.9

With the aforementioned strict definition of accuracy, which is an allowed error of three pixels in horizontal distance δ between the estimated IML and the ground truth, the accuracy of IML estimation in this system is 96.9%, which is higher than 95% reported in [9] as shown in Table 3.1.

Table 3.2 Comparison on the mean value of error for IML estimation

Method	Our method	Method in [93]	Method in [94]
Number of CT slices	280	23	23
Image format	JPEG	Analyze 7.5	Analyze 7.5
Mean value of error δ	2.1	2.9	3.5

We also compare our results with the work completed by other research groups. In order to evaluate the result of the mid-sagittal plane estimation, Ruppert *et al.* used an average z-distance measure to indicate the displacement between the resulting plane and the ground truth plane inside one image [93]. Therefore, the average z-distance measure has the similar physical meaning as the error δ in our method. The smaller the mean value of error δ, the closer the estimated IML is to the ground truth. As the comparison in Table 3.2, the mean value of the error δ in our method is only 2.1 pixels, which is much less than the ones reported in [93, 94]. The above experimental results demonstrate the high reliability of the proposed system.

3.4 Summary

In this study, we propose a system to identify the ideal midline using CT scans of the patients. With the assistance of CT Slice Selection Algorithm (SSA) in the previous chapter, ideal midline detection works only on a few most suitable slices. With the implementation of the exhaustive symmetric position search, an approximate ideal midline is detected. Using the position of the falx cerebri and protrusion of skull bone, the position of ideal midline is further refined. In order to enhance the accuracy of the ideal midline detection, the global rotation assumption fully considers the connection among CT slices and thereby compensates the error generated by using a single CT slice. The high accuracy of this system on ideal midline detection shows the potential for such a system to be implemented in clinical settings.

Chapter 4 Actual midline detection and midline shift estimation

4.1 Background and introduction

The degree of the midline shift is an important index for clinicians to assess the TBI severity and ICP level. The detection of the actual midline position is crucial in the estimation of midline shift. Using ventricle position to detect the actual midline is one of the most popular methods in detecting the MLS.

In detecting the brain midline shift, the image segmentation method is generally the most important step of detecting ventricles in a specific CT slice [9, 95-97]. A validation process is generally employed to re-examine and further refine the ventricle segmentation [94].

A model based on quadratic Bezier curve, to detect the actual midline shift is proposed by Liao *et al* [96]. In this method the CT image is divided into three parts. The central curve is formed by a quadratic Bezier curve in which the genetic algorithm is applied to prevent the Bezier Curve reaching a local minimum. Although the model is simple and effective, the accuracy of the method is reported to decrease sharply (down by 41% reported in [96]) on CT slices with spontaneous intracranial hemorrhage.

The linear regression model named H-MLS model is introduced by Liu. *et al.* [97] to simulate the relationship between the hemorrhage and the midline deformation. The midline shift (MLS) is predicted by the H-MLS model and is adjusted based on the symmetry information that is not always true in physical circumstances.

A known high-accuracy method for brain midline estimation utilizes the central position of the ventricle system as the midline estimate. Image segmentation methods based on statistical models have attracted a lot interest but have been notorious for being extremely time consuming during processing. Chen *et al.* proposed a method based on Gaussian Mixture Model (GMM) and template matching to detect the ventricle system on brain CT images. As aforementioned, in this method GMM [95] was utilized which provided better results as compared to ICM and MASP [9], however, Chen's result suffers high computation time and fails sometime in identifying ventricles boundary.

Segmentation based on active contour methods has attracted a great deal of attention in the past quarter century. In general, the active contour model has two categories: the parametric active contour model and the geometric active contour model. Kass *et al*. proposed the Snake model, namely explicit active contour model, to extract the objects of interest from the image [98]. Various Snake models have been proposed in different applications, such as edge detection, curve detection, segmentation, shape modeling, and visual tracking [99-105]. Although this family of parametric active contour models is effective for many applications, it suffers some inherent difficulties such as the required prior shape information, the manual accurate initialization, and the inseparable contours during the course of propagation [106-110].

Geometric active contour models [111] are widely used in medical imaging for segmentation of cerebral vessels, left ventricle of heart, as well as pelvic bone [112-114]. Caselles *et al.* [115] and Malladi *et al.* [116] introduced the implicit geometric active contour model based on curve evolution theory [117] and level set method [118]. In this group of geometric active contour model, the topology structure can be changed

automatically due to the implicit function's innate characteristics. Thereby solving the shortcoming of parametric active contour model where it fails to automatically separate curves. An intrinsic limitation of the traditional level set segmentation method is the re-initialization problem and its high sensitivity to local image intensities, which is overcome by the variational level set method. Li *et al.* [119-121] proposed a region-based active contour model with variational level set function using a distance regularization term. This method not only eliminated the need for re-initialization but also coped with the intensity inhomogeneity.

In this thesis, the region-based active contour model [120] is employed in the detection of ventricular tissue. In order to improve the detection results and speed up the contour evolution, a new proposed algorithm is used narrow the focus only to the region of interest before using image segmentation methods. After the segmentation, a ventricle identification process is used to estimate the actual midline and midline shift.

The rest of this chapter is structured as follows: In Section 4.2, the methodology of the proposed method is introduced. In Section 4.3, the result and discussion is given. The last Section gives the summary of the actual midline detection and midline shift estimation system.

4.2 Methodology

An illustration of the five major steps in the shifted midline estimation framework is shown in Figure 4.1. First, Window Selection Algorithm is run on the CT slices selected by the SSA algorithm to confine the region of interest. Weighted median filtering is then applied to remove noise and speed up the subsequent segmentation step. Utilization of the

level set segmentation effectively extracts potential ventricle contours in the WSA window. Subsequently, Ventricle Identification Algorithm employed as post-processing step to identify the right and left lateral ventricles. Lastly, the brain midline is estimated using the position of the ventricles. The following section will describe the details of each step.

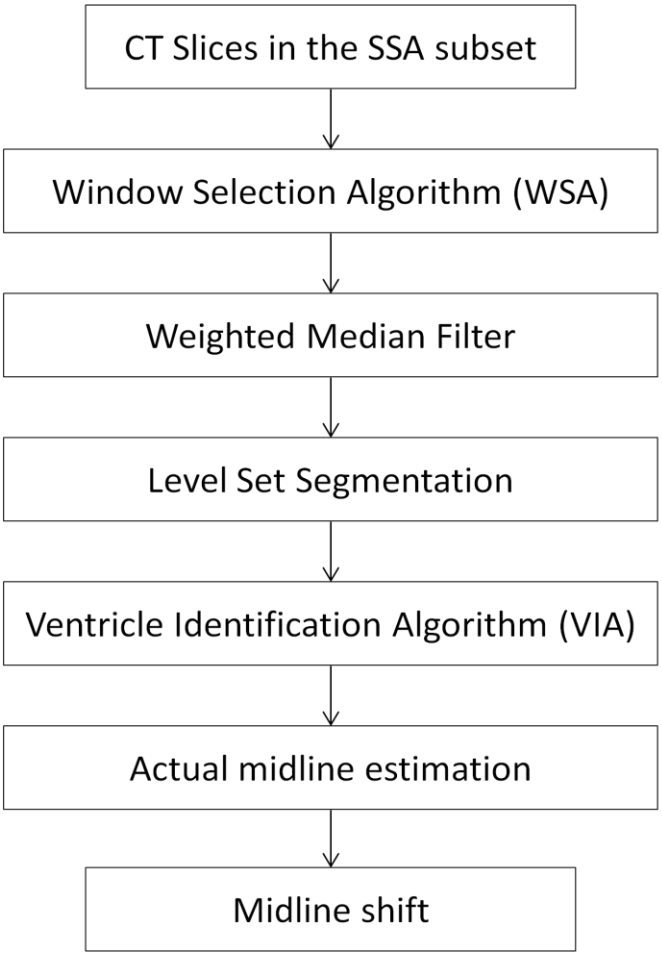

Figure 4.1 Schematic diagram of the five-step algorithm for actual midline estimation

4.2.1 Window Selection Algorithm

In order to provide the initialization for level set segmentation and reduce time complexity of the algorithm, a new algorithm, named Window Selection Algorithm (WSA), has been proposed in this work. This algorithm helps chooses the best suitable slice from the SSA subset and confines the region of interest for segmentation within a dynamic selected window.

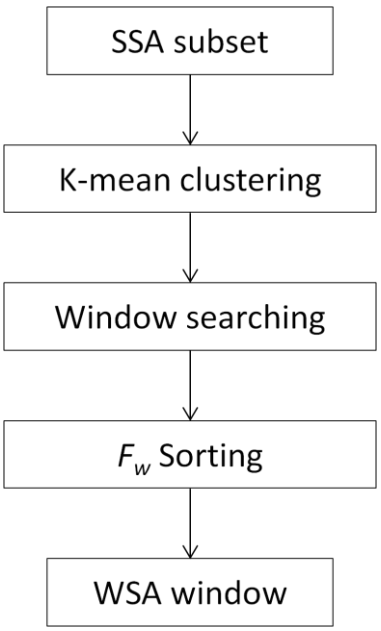

Figure 4 2 Schematic diagram of Window Selection Algorithm

The implementation of the WSA algorithm begins with an initial window setting on the CT image. Here the calibrated ideal midline (see chapter 3) acts as a guide in the initial seed window choosing. Starting with this initial window, the WSA algorithm scans the image to choose the most suitable window within each CT slice. Subsequently, comparison is made among the selected windows from each CT slice in the SSA subset,

using which the WSA algorithm selects the best slice with the window of interest which adequately represents the ventricle structure as the initialization for segmentation.

The figure 4.2 shows the WSA algorithm schematic diagram. It should mention that WSA algorithm works on the SSA subset in which every CT slice has been calibrated to its center after ideal midline detection. Therefore, another K-mean clustering should be applied as we did in SSA algorithm (Chapter 2) in which the pixels related to lowest intensity center are labeled as belonging to the ventricle class. As aforementioned, the WSA algorithm is designed to confine the region of interest. Since the speed of the contour evolution in the following level set segmentation depends on the image size to a great extent, narrowing down the region of interest only to the area containing the ventricles can effectively accelerate the algorithm. Based on the anatomical characteristics and the experimental results, we set the seed window to an appropriate default size which is 85*115 pixels (width*height) in this work. The WSA algorithm scans the seed window within the intracranial region to select the appropriate window with the most ventricle pixels on each slice. To indicate the likelihood of a window containing ventricles, a new measure, called Window Fidelity Measure (F_w), is proposed. Window Fidelity Measure is defined by the percentage of pixels belonging to the ventricles inside the window. With the implementation of the seed window scan on all slices in the slice subset, the maximum Window Fidelity Measure (max-F_w) and the related window position of every slice are calculated. By sorting those max-F_w values, the best candidate slice with the top F_w value is selected for execution of the following segmentation.

In addition, considering just the discrete points within the window independently is not so meaningful in practice. It is more important is to consider the points set composed of connected components as the candidate object of study. Thus, Connected Component Algorithm (CCA) was employed before the window scan in the WSA algorithm to eliminate the noise, namely those discrete points or tiny point-groups which were wrongly labeled as possible ventricles. Using CCA, those regions that fall below the threshold size of connectedness (60 pixels in this work) are considered to be too small and thus discarded.

Therefore, the WSA algorithm not only selects the best candidate slice but also confines the working region only to the most suitable window.

4.2.2 Weighted Median Filter

Prior to level set segmentation, image filtering for noise removal is normally recommended. Image noise can indirectly increase the computational costs and therefore increase time in the segmentation step by increasing the number of iterations. In addition, some images fail to be segmented due to the noise. Furthermore, during the ventricle identification step, the less noise the image has, the more efficient and accurate the algorithm possess. In this work, weighted median (WM) filter is used to remove noise further before segmentation. The weighted median filter is a natural extension of the median filter [122]. WM filter still keeps the advantage of the median filter and is more reliable by giving more emphasis to detail information of the sample. With the weights, the WM filter can be better to preserve desired signal structures than median filter [123]. For a median filter with a window width 2k+1, the details only are preserved at most k+1

points. Since a smaller window is always needed for preserving smaller details in signals, the noise could not be reduced effectively in median filter method [122]. The WM may resolve this dilemma using a long enough window and weights set. Firstly, the noise can be suppressed effectively by a longer window. Secondly, the weight can preserve details lasting less than k+1 points. Some versions of the WM filter have already been widely applied in image processing [124-126]. The justification of using median filtering techniques has been discussed further in the result section 4.3.

4.2.3 Ventricle segmentation based on level set method

The level set method represents contours as the zero level set of an implicit function defined in a higher dimension, usually referred to as the level set function, and to evolve the level set function according to a partial differential equation [127]. Generally, there are two kinds of active contour models, the parametric active model and the geometric active model. Comparing to geometric active contour, the parametric active contour such as Snake Model [98] fails to adapt the contour to topological change. Geometric active model implemented by level set method is known as the variational level set method [108, 128]. In this work, the region-based geometric active contour model in [120] is used owing to its two benefits: (1) it avoids the expensive re-initialization of the level set function after some iterations and (2) it has reduced sensitivity for non-homogeneous images.

Here, we consider a two-dimensional gray level image I: $\Omega \rightarrow \Re$, where $\Omega \subset \Re^2$ is the image domain and I is the image intensity [120]. C represents closed contour in the 2-D image domain ($C \subset \Omega$) and segments the image into two regions: $\Omega_1 = \text{outside}(C)$ and

$\Omega_2 = \text{inside}(C)$. The contour C is represented by the zero level set of a Lipschitz function $\varphi: \Omega \to \Re$, which is a level set function. The energy function $\mathcal{F}(\varphi, f_1, f_2)$ subject to minimization is defined as

$$\mathcal{F}\big(\varphi, f_1(x), f_2(x)\big) = \mathcal{E}\big(\varphi, f_1(x), f_2(x)\big) + \mu\mathcal{P}(\varphi) \qquad \text{Eq. 4-1}$$

where the external energy $\mathcal{E}\big(\varphi, f_1(x), f_2(x)\big)$ drives the zero level set towards the object boundaries, while the internal energy $\mu\mathcal{P}(\varphi)$ penalizes the deviation of φ from a signed distance function during its evolution. The external energy can be rewritten as below,

$$\begin{aligned}\mathcal{E}\big(\varphi, f_1(x), f_2(x)\big) &= \mathcal{E}_f + v|C| \\ &= \sum_{i=1}^{2} \lambda_i \int \Big(\int K_\sigma(x-y)|I(y) - f_i(x)|^2 M_i(\varphi(y))dy\Big)dx \\ &\quad + v\int |\nabla H(\varphi(x))|dx \qquad \text{Eq. 4-2}\end{aligned}$$

where the fitting energy $\mathcal{E}_f$ minimizes the gray value variance in the separated phases and the contour length $|C|$ smoothes the curve. In Eq. 4-2, *x* and *y* is used to describe the pixel location, the kernel function K_σ represents a 2-D Gaussian kernel with $K_\sigma(u) = \frac{1}{(2\pi)\sigma^2} e^{-\frac{|u|^2}{2\sigma^2}}$ (σ is positive constant), λ_1 and λ_2 are constants in the fitting energy item, *v* is a constant in the contour length item, and *I(y)* indicates the image intensity. The fitting functions $f_1(x)$ and $f_2(x)$ reflect the intensity in the region with center *x* and can be calculated as below,

$$f_i(x) = \frac{K_\sigma(x) * [M_i(\varphi(x))I(x)]}{K_\sigma(x) * M_i(\varphi(x))}, (i = 1, 2) \qquad \text{Eq. 4-3}$$

where the operator * denotes convolution. Using the fitting function makes the variational level set method tolerant to the non-homogeneity in images to some extent. $M_i(\varphi)$ is defined by

$$M_i(\varphi) = (2-i)H\big(\varphi(x)\big) + (i-1)\Big(1 - H\big(\varphi(x)\big)\Big), \ (i = 1, 2) \qquad \text{Eq. 4-4}$$

where the Heaviside function H is approximated by a smooth function $H_\varepsilon(x)$ and given as below,

$$H_\varepsilon(x) = \frac{1}{2}\left[1 + \frac{2}{\pi} arctan\left(\frac{x}{\varepsilon}\right)\right] \quad \text{Eq. 4-5}$$

The derivation of $H_\varepsilon(x)$ is as follows.

$$\delta_\varepsilon = H_\varepsilon'(x) = \frac{1}{\pi}\frac{\varepsilon}{\varepsilon^2 + x^2} \quad \text{Eq. 4-6}$$

The internal energy $\mu\mathcal{P}(\varphi)$ in Eq. 4-1 consists of a constant μ and a level set regularization term $\mathcal{P}(\varphi)$.

$$\mathcal{P}(\varphi) = \int \frac{1}{2}(|\nabla\varphi(x)| - 1)^2 dx \quad \text{Eq. 4-7}$$

This regularization item $\mathcal{P}(\varphi)$ helps stabilize the curve evolution and avoids the time consumption due to re-initialization, which is the highlight of the variational level set method used in this work.

With a fixed f_1 and f_2, the energy function $\mathcal{F}(\varphi, f_1, f_2)$ in Eq. 4-1 can be minimized by solving the gradient flow equation as follows:

$$\frac{\partial\varphi}{\partial t} = -\delta_\varepsilon(\varphi)\left(\lambda_1 \int K_\sigma(x-y)|I(x) - f_1(y)|^2\, dy - \lambda_2 \int K_\sigma(x-y)|I(x) - f_2(y)|^2\, dy\right)$$
$$+ v\delta_\varepsilon(\varphi) div\left(\frac{\nabla\varphi}{|\nabla\varphi|}\right) + \mu\left(\nabla^2\varphi - div\left(\frac{\nabla\varphi}{|\nabla\varphi|}\right)\right) \quad \text{Eq. 4-8}$$

with

- $-\delta_\varepsilon(\varphi)(\lambda_1 \int K_\sigma(x-y)|I(x) - f_1(y)|^2\, dy - \lambda_2 \int K_\sigma(x-y)|I(x) - f_2(y)|^2\, dy)$ is the data fitting term;
- $v\delta_\varepsilon(\varphi) div(\frac{\nabla\varphi}{|\nabla\varphi|})$ represents the arc length term
- $\mu(\nabla^2\varphi - div(\frac{\nabla\varphi}{|\nabla\varphi|}))$ is the level set regularization term

The segmentation used in this work is based on the level set evolution Eq. 4-8. Further details can be found in reference [120].

The terminal condition of curve evolution determines the number of iterations and segmentation accuracy. In this work, the contour length difference between iterations is used as the terminal condition of the evolution. When the absolute difference between the current and the previous contour length is less than a default threshold S (S=3 pixels in this work), the curve evolution is close to stable on this iteration, as shown in Eq. 4-9.

$$\big||C(t)| - |C(t-1)|\big| < S \qquad \text{Eq. 4-9}$$

Owing to the complexity of the medical image, it is possible that some iteration curve satisfying Eq. 4-9 only represents a slow-down in evolution but is still far away from reaching the real object boundary. Using an uninterrupted iteration time to guarantee the stability of the evolution is necessary for a robust terminal condition. Therefore, we set T times (T=20 in this work) evolutions continuously satisfying Eq. 4-9 as the terminal condition of the curve evolution. This ensures that the terminal condition will not be reverted in the next iteration.

Using level-set segmentation in combination with the terminal condition as discussed above, potential ventricle contours are extracted from the WSA window on the candidate CT slice. Generally, two ventricle contours should be found corresponding to the right and left lateral ventricles. However, due to the complexity of CT images, in practice, less than or more than two contours are possibly found by the level set segmentation. Therefore, we need the following ventricle identification process to identify the actual ventricles.

4.2.4 Ventricle identification and actual midline estimation

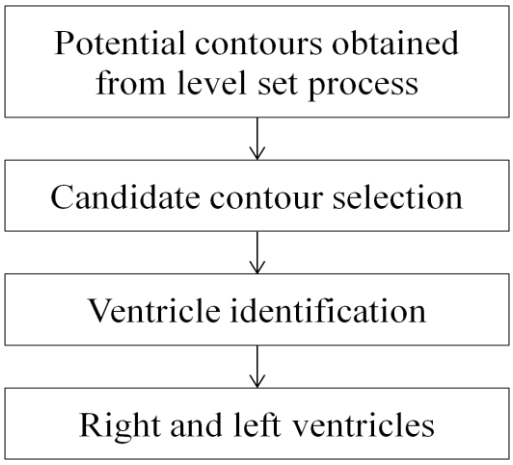

Figure 4.3 Schematic diagram of Ventricle Identification Algorithm

Following ventricle segmentation, Ventricle Identification Algorithm (VIA) is proposed to identify the actual right and left lateral ventricles for subsequent actual midline estimation process.

As the schematic diagram in Figure 4.3 illustrates, the first step of VIA is to select candidate contours from a set of contours obtained from level set segmentation. Here, the candidate contours are the contours with high probability of representing the actual right and left lateral ventricles. Based on experience, unclosed contours and contours with short lengths should be removed. We use the Connected Component Algorithm (CCA) [84] to remove the unclosed contours. Separately, a threshold method is used to remove the shortest contours. Setting a contour-length threshold of l_c ($l_c = 60$ pixels in this work), any contour with the length less than l_c is removed directly by thresholding. In addition, if the number of the contours is still greater than three, after the above selection,

three contours with the longest length are selected as the candidate contours. Therefore, the number of candidate contours should be equal to or less than three.

The following ventricle identification is based on the number of candidate contours and their mass center positions. The mass center calculation method is introduced in Chapter 2. Thus, the coordinate of the mass center (x, y) of the contour can be obtained by

$$\begin{cases} x = \frac{m_{10}}{m_{00}} \\ y = \frac{m_{01}}{m_{00}} \end{cases} \quad \text{Eq. 4-10}$$

where the moment m_{pq} is defined in Eq. 2-13.

The ventricle identification can be categorized into four cases, each defined by a different number of candidate contours. After the candidate contour selection, there are only three or less than three candidate contours left. If no candidate contour is found, it means that no ventricle is recognized in this CT slice. The algorithm will automatically go back to the WSA algorithm and execute on the second candidate slice. If only one candidate contour is found, either one ventricle is missing from the window or the two ventricles are being displayed as one messed up. In this case, it is hard to estimate the actual position of the two ventricles and the midline of the brain. Thus, the VIA algorithm automatically skips the slice with only one candidate contour and moves back to WSA for the next candidate slice. If two candidate contours are found, VIA identifies the right and left lateral ventricles by comparing the mass center positions of the two contours along the x direction. However, if three contours are found, the contours' mass center information is used to confirm the right and left lateral ventricles. Details of VIA in this case will be discussed in Section 4.3. Figure 4.3 illustrates how the VIA algorithm is used to identify the right and left lateral ventricles.

After ventricle identification, the actual midline can be estimated as follows. Assume that the right and left lateral ventricles have mass center positions (x_L, y_L) and (x_R, y_R), respectively. The brain actual midline is then estimated to be at middle of the two ventricles and have the slope K given by Eq. 4-11.

$$K = -tan\frac{(x_2 - x_1)}{(y_2 - y_1)} \quad \text{Eq. 4-11}$$

4.3 Results and Discussion

4.3.1 Data

This database contains original 3133 axial CT scan slices acquired across 70 patients with cases of both mild and severe Traumatic Brain Injuries (TBI). All the 280 CT scans from SSA subset have been utilized to detect the actual midline and estimate the brain midline shift.

4.3.2 Results and discussion

4.3.2.1 Results of Window Selection Algorithm implementation

Window Selection Algorithm (WSA) is aimed at selecting the most appropriate slices and confining the window of focus. Figure 4.4 shows the results of implementing WSA on one patient's CT images. The four CT slices in Figure 4.4-a are the ones selected by the SSA algorithm. With the WSA algorithm, these slices are sorted by their F_w value. The higher Window Fidelity Measure is, the clearer and more accentuated the ventricles are in the window. As shown in Figure 4.4-b, the CT slice with top F_w is selected as the first

candidate slice with its suitable window. As it can be noticed, it successfully provides a reasonable initial contour for the segmentation step.

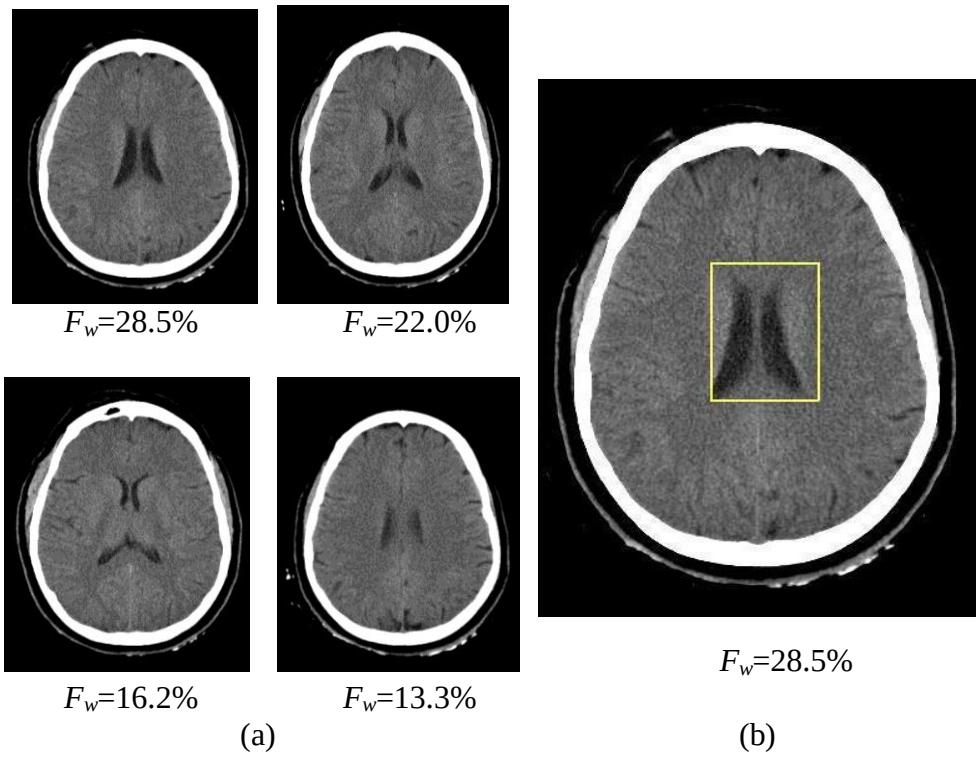

Figure 4.4 The results for Window Selection Algorithm implemented on the four slices selected from one patient's CT scan by the SSA algorithm. (a) Slices sorted by F_w, (b) the first candidate slice with WSA window.

By confining the region of interest to only the WSA window, the time cost associated with level set segmentation is greatly reduced. Additionally, the contour evolution becomes more efficient due to avoidance of the side effects produced from regions outside the window. As a result, the first candidate slice with its WSA window attains a very high probability of success in the remaining steps. In our study, for 52 out of 65 cases, in which the ventricle boundaries are correctly extracted with segmentation, we obtain the actual midline using the WSA slice with top F_w.

4.3.2.2 Results of Weighted Median Filter implementation

After extensive experimentation, we find that performing a weighted median filter operation on the CT scan prior to the level set evolution can be useful. The weighted median filter smoothes out noise from CT image, avoiding noisy contours in the segmentation results.

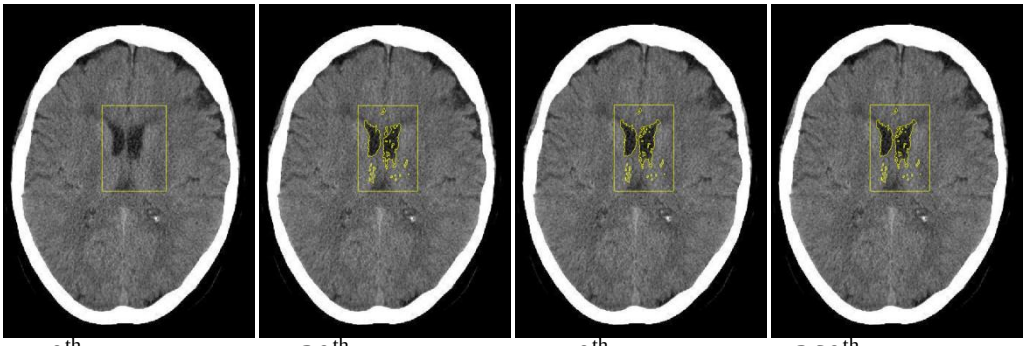

0^{th} iteration 30^{th} iteration 120^{th} iteration 360^{th} iteration

(a)

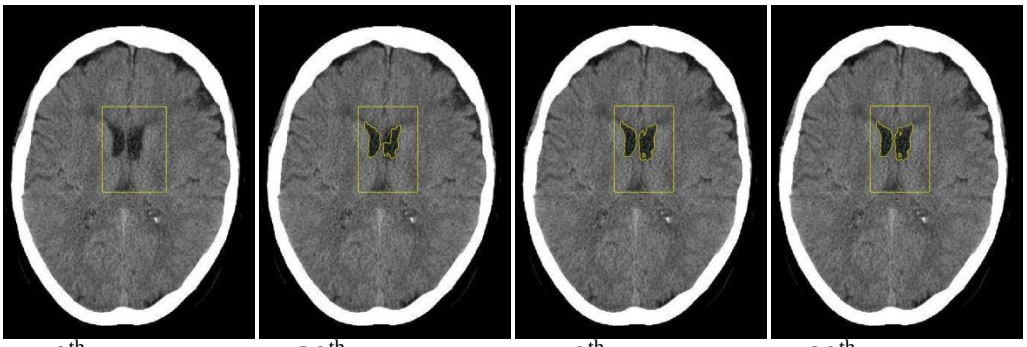

0^{th} iteration 30^{th} iteration 120^{th} iteration 180^{th} iteration

(b)

Figure 4.5 Contour evolution on a CT image with and without weighted median filter implementation prior to the level set segmentation. (a) Contour stability occurs after 360 iterations without weighted median filtering, (b) contour stability occurs after 180 iterations when weighted median filtering is applied.

However, the most important benefit of weighted median filter in the framework is the major reduction in segmentation time. As shown in Figure 4.5, weighted median filtering decreases from 360 to 180 the number of iterations required for contour stability. Fewer itterations result in a speed-up in the implementation of the algorithm. More, very few noise contour remians in the window when weighted median filter applied prior to the contour evolution (Figure 4.5, bottom row). Without weighted median filter, several noise contours appear (Figure 4.5, top row) which will seriously affect the following ventricle identification. Based on our database of 70 patients, an average of 160 iterations are required to complete contour evolution with filtering, while an average of 280 iterations were required without filtering.

4.3.2.3 Results of Level Set Segmentation implementation

The initial level set function φ assigns the value 2 for all the pixels within the WSA window. The value of φ here is chosen arbitrarily and can be any value between 0-255 (pixel intensity values). The parameters of the level set function are set as follows, $\lambda_1 = 1$, $\lambda_2 = 1$, $\sigma = 3.0$, time step $\Delta t = 0.1$, $\mu = 1$ and $v = 0.001 \times 255 \times 255$.

Figure 4.6 depicts the results of the level set method at different iterations, from the initial stage to the final stable contour within the WSA window. In Figure 4.6, the sub-images from top left to right shows results after 0, 30, and 50 iterations of the level set evolution, respectively; while the bottom sub-images from left to right shows results after 100, 150, and 200 iterations of the level set evolution, respectively. Satisfying the terminal condition, wherein all the boundaries of the ventricles have been sucessfully identified, the evolution becomes stable after 200 iterations. Figure 4.7 shows the 3-D

final level set function. Its contour on the zero-plane is actually the final 2-D contour shown in the bottom-right sub-image in Figure 4.6. It can be seen that the level set segmentation successfully extracts the ventricle boundaries which feed the ventricle identification and brain midline estimation steps.

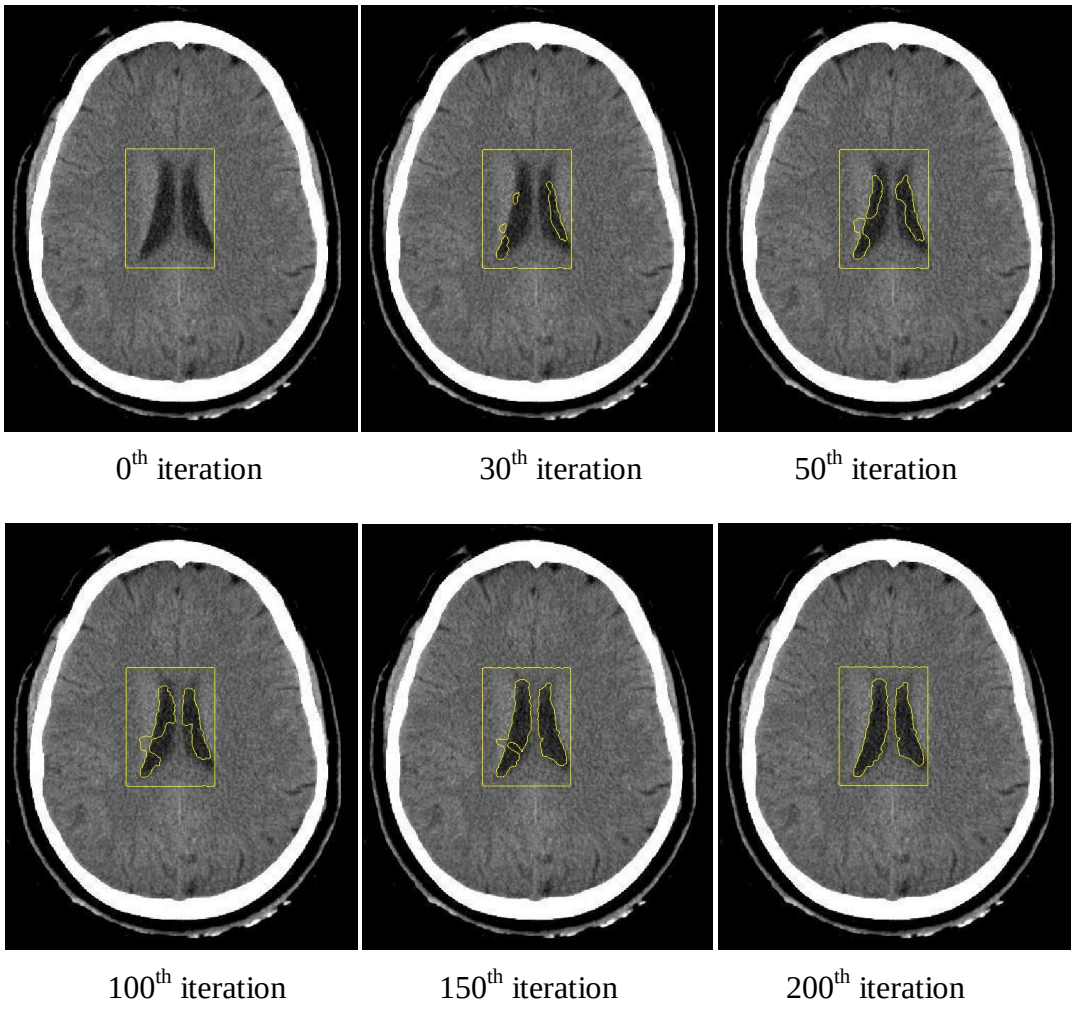

Figure 4.6 Contour evolution using the level set algorithm at different levels of iteration (0, 30, 50, 100, 150, and 200 iterations for the sub-images from the top left to bottom right)

The segmentation algorithm was implemented in Matlab on a PC with Intel core i7 3.40 GHz processor and 8GB of RAM. The average CPU time for the level set evolution on a single candidate CT slice was 129.2 seconds. We compared our level set results with those by the Gaussian Mixture Model (GMM) method [95] using the same database. We found that the level set segmentation took 20% less time compared to the GMM method.

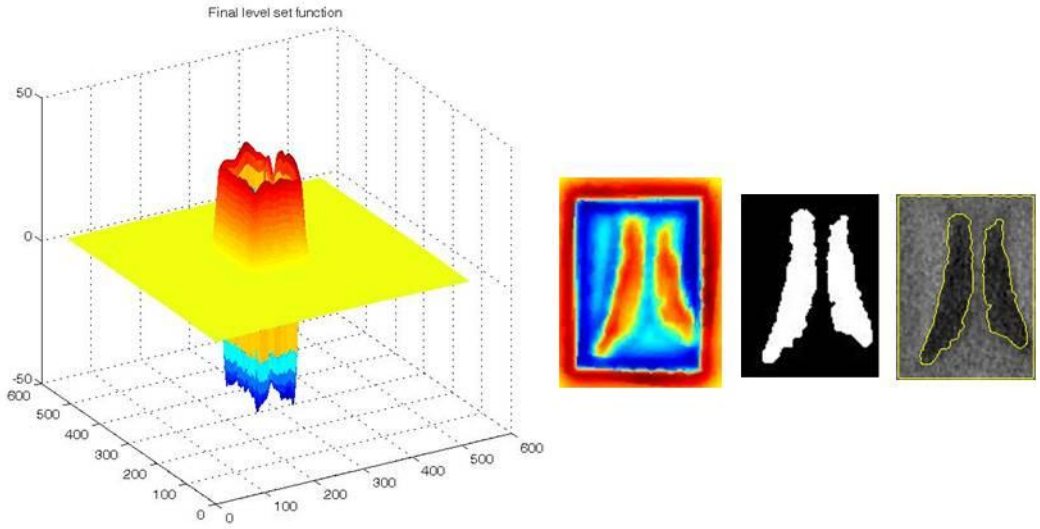

Figure 4.7 The 3-D level set function with the zero plane when contour stability

4.3.2.4 Ventricle identification and actual midline detection

Following level set segmentation, in most cases, there are two possible contours extracted from the WSA window. Based on Ventricle Identification Algorithm (VIA), the two candidate contours indicate the right and left lateral ventricles. For the case with more than three contours, the largest three contours are selected as the candidate contours at the beginning of VIA process. Figure 7 presents the ventricle identification and midline estimation process for the case with three candidate contours. Figure 7-a shows that three

candidate contours are extracted by VIA. According to the positions of the mass centers and the size of the three candidate contours, VIA selects two of them to represent the left and right lateral ventricles. For instance, with three contours if two of them have similar mass center positions and similar lengths, while the third contour is different from these two in both size and position, then the two similar contours are selected as the ventricle contours. The top small contour in Figure 4.8-a should be removed from the list of candidate contours if compared to the bottom two contours (Figure 4.8-b). The mass centers of the selected ventricle contours are then calculated by Eq. 4-10 (Figure 4.8-c). According to the positions of the ventricle mass centers, the actual midline is estimated as shown in Figure 4.8-d.

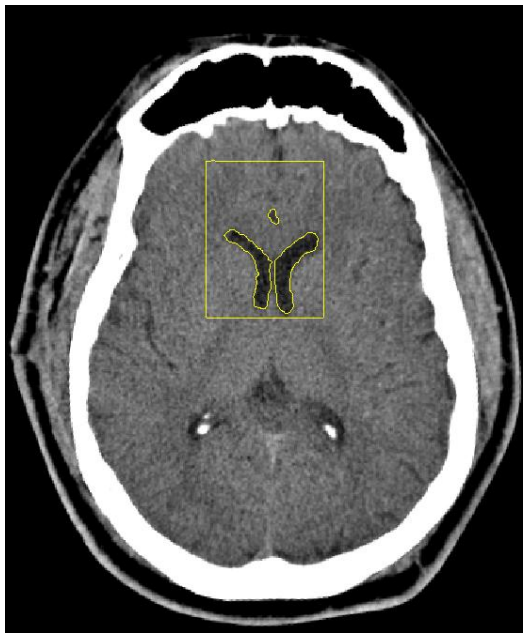

(a)

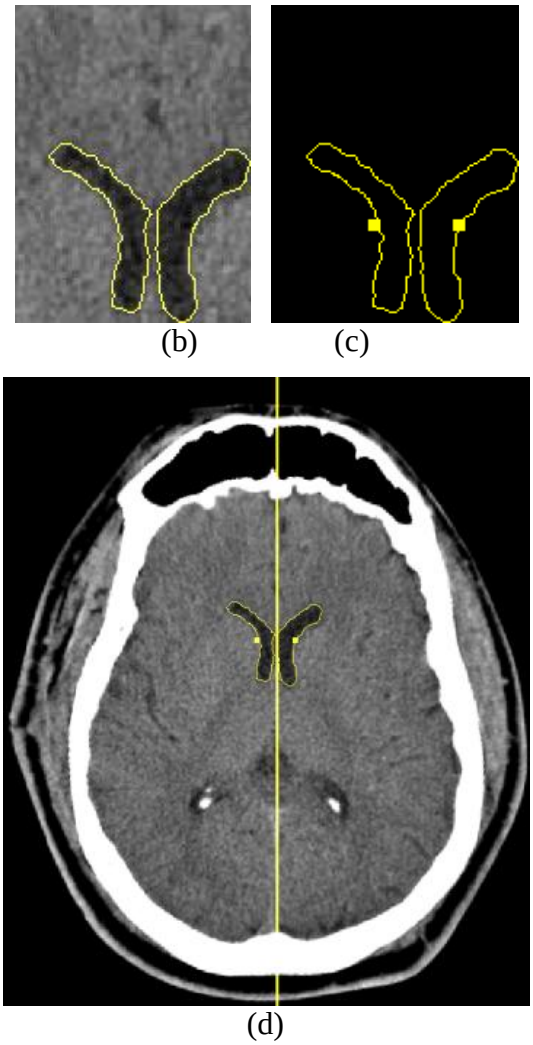

Figure 4.8 Ventricle identification and brain midline estimation. (a) Three candidate contours, (b) identification of two ventricle contours, (c) centers of mass of the ventricle contours, (d) midline estimation.

The collaborating physician manually labeled the actual midline for every patient in the database. With a strict definition of accuracy, which is an allowed error of three pixels in the horizontal direction and 2 degrees of the rotation angle, the accuracy of the midline estimation of our system is 92.5%, higher than 87.5% reported using GMM method in [95]. In the GMM method, the accuracy was measured using only the horizontal direction

shift of three pixels, whereas in this proposed method, the inclusion of rotation angle into the definition of accuracy makes the accuracy criterion stricter.

4.3.2.5 Brain midline shift estimation

Figure 4.9 Midline shift estimation. The red line represents the ideal midline and the yellow line represents the actual midline. The horizontal distance of their mass centers is the brain midline shift.

The ideal midline can be detected using the process introduced in Chapter 3, and the actual midline is detected using the process introduced in this Chapter. Then the brain

midline shift s can be calculated by the horizontal difference of the above two lines as follows.

$$s = |x_{ideal} - x_{actual}| \quad \text{Eq. 4-12}$$

where x_{ideal} is the x coordinate of the mass center of the detected ideal midline and x_{actual} is the x coordinate of the mass center of the detected actual midline. Figure 4.9 shows the midline shift estimation on one CT slice.

4 .4 Summary

In this chapter, an actual midline detection system based on a variational level set segmentation method is described and the midline shift estimation is presented. During the pre-processing step, a window selection algorithm (WSA) selects the appropriate CT slice containing clear ventricle information and confines subsequent operations within a specific window. WSA greatly enhances the efficiency of the whole system by reducing segmentation time. The use of the variational level set segmentation model combined with the ventricle identification algorithm successfully extracted ventricle contours. Actual midline was detected using the centers of mass of ventricle contours. The actual midline estimation technique achieved an accuracy of 92.5% after validation by a physician. Hence, this framework shows to be a viable tool to aid clinicians in assessing severity of TBI using brain midline shift detection.

Chapter 5 Application: Intracranial Pressure Prediction

5.1 Background and introduction

The elevation of intracranial pressure (ICP) is one of the most serious problems associated with traumatic brain injury (TBI) which is a major medical and socioeconomic problem. ICP may cause brain swelling accompanied by elevated ICP can result in inadequate cerebral perfusion with well-oxygenated blood and potentially deadly consequences such as ischemia, herniation, and reflex bradycardia [129, 130]. ICP monitoring is a standard procedure in the care of severe TBI patient [6, 131]. The ability of non-intrusively conduct a pre-screening of ICP can be very helpful in avoiding invasive procedures which could lead to infection and further damage to the brain tissue.

In this work, a non-intrusive ICP prediction model has been proposed to assist physicians during the assessment of the severity of TBI. The prediction model built in our previous work [132] has been modified in this study and was updated using multiple valuable new features as input to the classification model. The validation result of the developed model shows that the proposed method could potentially be used as a reference during the decision support process before intensive brain surgery.

5.2 Methodology

5.2.1 Candidate features

The symptoms observed due to increased ICP levels are usually shifted brain structures, hydrocephalus, herniation, and intracranial hematoma [133]. These symptoms can be

directly translated into a series of features extracted using advanced image processing techniques, such as midline shift, abnormal intracranial air, cerebrospinal fluid (CSF) size, and changes in the brain matter texture patterns. The extracted features are then used as an input in developing prediction models towards estimating the level of ICP in a given patient. Furthermore, the proposed prediction system also utilizes demographic information such as patient age, and other clinical measures such as Injury Severity Score (ISS). The details of extracting these feature sets have been discussed below.

5.2.1.1 Brain midline shift

MLS is an important index for clinicians to assess the severity of TBI. MLS is known to be highly correlated with the ICP levels [9]. The midline shift can be estimated according to the method introduced in Chapter 4.

5.2.1.2 Ventricle Size

The ventricles in the brain of a young adult are well-developed and filled with cerebrospinal fluid (CSF). They are open but not excessively large. In CT images, ventricles display near black in the center of brain. Figure 5.1 shows a brain CT slice with normal sized ventricles. During cases of cerebral atrophy, the size of the ventricles increases thus making it a valuable feature for ICP prediction.

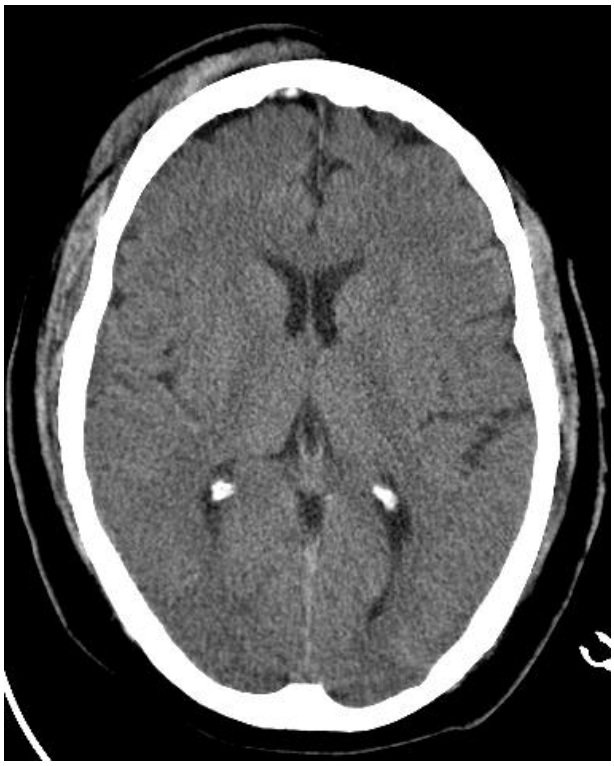

Figure 5.1 A brain CT slice with normal ventricles

Ventricle size feature can be measured in multiple ways. One is using the area of the extracted contours of left and right lateral ventricles by the method introduced in Chapter 4. Another is to use template matching algorithms during ventricle identification in CT slices [9]. It can also be evaluated by computing the ratio between the number of ventricle pixels and the total number of intracranial pixels.

5.2.1.3 Intracranial air cavities

In cases of a head injury, air cavities may form inside the intracranial region (Figure 5.2). Air can leak into the cranial chamber through the mastoid and/or associated temporal bone fracture [85]. Since air cavities are unusual inside the skull, detecting them can valuable information in predicting the ICP levels. The sizes of the air cavities may vary

from small air bubbles to larger air pockets. More detail introduction of the intracranial air can be found in Section 2.2.5.

Figure 5.2 Brain CT image with air in intracranial region

Intracranial air appears black on all CT images. For instance, the black region close to the calvaria in Figure 5.2 is the intracranial air. To measure this feature, we extract all intracranial pixels with the intensity in the range of 0-5 (out of 255) using a threshold based techniques. Furthermore, the intracranial region can be obtained by the following steps, (1) extract skull bone from the CT image using threshold based method, (2) obtain the region inside by skull bone (3) calculate the mass center of skull bone (4) identify the intracranial region that contains the position of the mass center of the skull bone.

5.2.1.4 Blood Amount Estimation

Figure 5.3 A sample slice with hemorrhage

Another useful feature is the estimation of the collected blood volume due to hematoma or hemorrhage. Figure 5.3 shows a patient suffers from the large amount extra blood (hemorrhage) in intracranial region. Excessive accumulation of blood can also be a cause in the displacement of brain tissues and increase in ICP levels. The measurement of blood amount can be implemented by the Gaussian Mixture Model (GMM) segmentation [134].

5.2.1.5 Texture Feature

Identifying the texture of the brain matter also can be used towards ICP prediction. In the case of elevated ICP, the texture of gray matter and white matter may change due to compression, which may result in the change of their appearance.

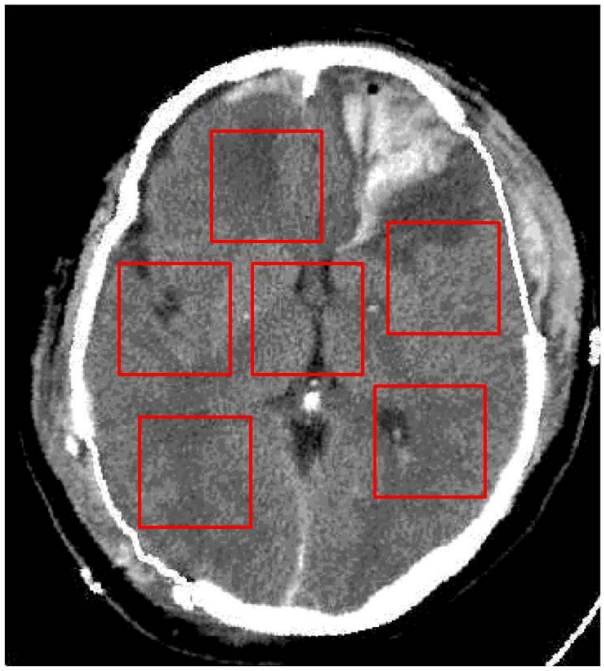

Figure 5.4 Texture feature extraction using six rectangular windows on one slice.

As shown in Figure 5.4, to measure the texture feature, six rectangular sub-images (windows) are selected on each CT slice to contain the brain tissue in the intracranial region, while avoiding the region of blood and ventricles. Two sets of texture feature are used in this work [135, 136]. The first set is generated using histogram with 10 bins. Texture features are expressed by the variance of those histograms. A new feature, σ^2, is produced in this process, where σ is the standard deviation of the window region.

Another new feature, called the measure of smoothness *r*, can be calculated using the following equation;

$$r = 1 - \frac{1}{1 + \sigma^2} \qquad \text{Eq. 5-1}$$

The value of *r* is in a range of 0 to 1. The lesser the value of r, the smoother is the texture of that region.

The second set of texture features is computed using Grey Level Run Length Method (GLRLM) [137], which extracts higher order statistics of the texture using a matrix $R(\theta) = [r(i, j|\theta)]$. The element $r(i, j|\theta)$ shows the number of consecutive runs of length j at gray level i in the direction θ (0, 45, 90 and 135 degrees are used in this work). By using different weighting scheme, eleven features can be extracted from the matrix to represent the regularity and periodicity of the image.

5.2.1.6 Demographics and other patient information

Demographics such as patient age and gender, and other injury scores such as Injury Severity Score (ISS) provide extra information in prediction of ICP level. Patient's age is considered as main demographic information. Injury Severity Score (ISS) as a main measure of injury severity, which is also selected as a feature.

5.2.1.7 Feature Aggregation across CT slices

In order to consider the interplay among consecutive slices of each patient, all of the above mentioned features are aggregated for all the slices available of each patient which produces a series of new aggregation features for that patient.

To aggregate the extracted features, a statistical approach is used in the calculation. Specifically, *min*(*f*), *max*(*f*), *median(f*), *mean*(*f*), and *std*(*f*) are calculated and used as new aggregation features in ICP prediction. In the case of blood amount feature, in addition to the above aggregation features, *sum*(*f*) is also calculated. This aggregation process also integrates the features among different selected windows on the same CT slice. The final statistical features are expected to represent the state of a set of CT slices. Table 5.1 shows the number of candidate features in the CT scan of one patient.

Table 5.1 Candidate features of one patient's CT scan

Feature type	number of feature
Midline shift, ventricle size, intracranial air, and blood amount	30
Demographic information	2
Texture patterns	220
Total Number	252

5.3 Results and discussion

5.3.1 Data

The dataset used in this study contains 57 CT scans from 17 patients with mild to severe TBI. Some patients have more than one set of CT scan obtained during their hospital stay. With each set of CT scans, 5 CT slices with clear visibility of ventricles are used in this work because the features of these regions are used in the analysis. Thus, in effect 285 CT slices are used towards the final analysis.

For reference and validation purposes, the ICP value which was invasively measured for each patient is used towards the development and validation of the prediction models. The mean value in the two ICP measurements before and after the collection of CT scan is used as the reference ICP value for each case. In this work, there are 33 cases under normal ICP value (ICP$\leq$ 12) and 24 cases with elevated ICP (ICP$>$ 12).

5.3.2 Results and Validation

Since hundreds of features are computed by the proposed algorithm, it is vital to identify the subset of features that truly contribute towards ICP prediction. A wrapper model incorporating a classifier and a features selection method is employed in this proposed method in order to increase the accuracy of the model and to reduce inter-case variability. A two step process is used to select the subset of features from the large candidate set [138]. In the first step, a filter-like feature selection method is used to rank all features. Then features with higher rank are selected as the refined candidate sets. In the second

step, a wrapper feature selection method with a classifier is utilized to select the final feature set which improves the classification accuracy.

Information Gain Ratio criterion is utilized to select the top ranked 50 features in the first stage. The Information Gain Ratio is as follows,

$$GainR(C,A_i) = (H(C) - H(C \mid A_i)) / H(A_i) \qquad \text{Eq. 5-2}$$

where $H(C)$ is the entropy of class label, $H(A_i)$ is the entropy of attribute A_i, and $H(C|A_i)$ is the conditional entropy. Genetic search is used to further optimize the feature selection subset in the second stage. The population size is set to 5 and the maximal number of generation is set to 10. The evaluation criterion for each feature subset is 10-fold cross validation with support vector machine (SVM). In order to perform parameter search of SVM, another 10-fold cross validation is nested into the genetic search.

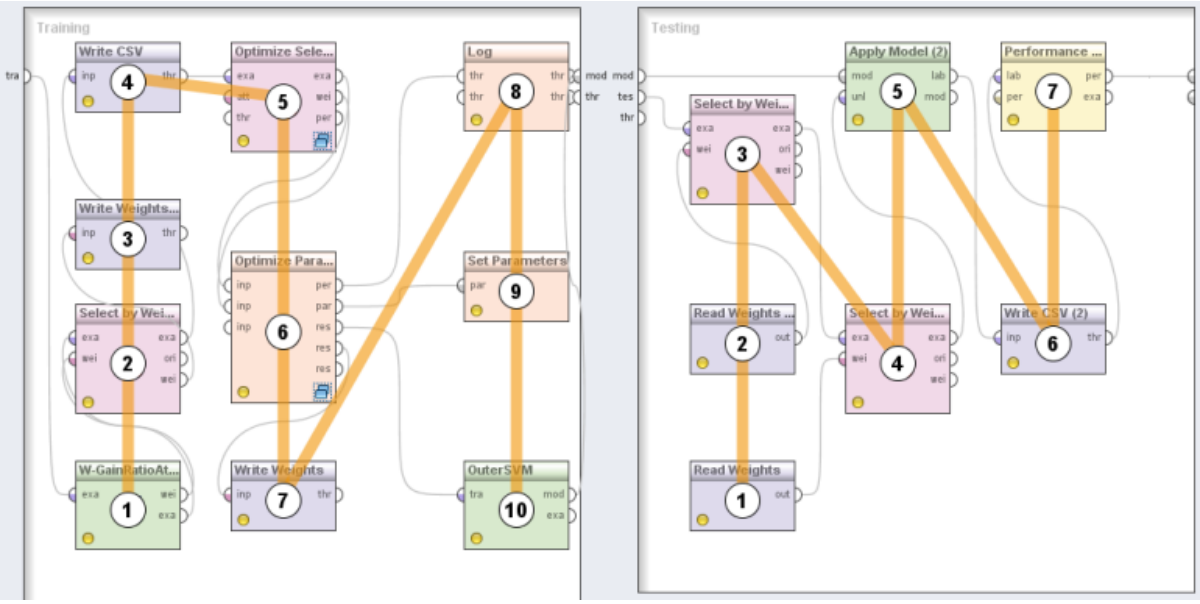

Figure 5.5 Top level cross validation in RapidMiner

The classification process is designed and run in RapidMiner [139] which provides a very intuitive graphic interface to design complex nested model and evaluation processes for classification purposes. Figure 3 shows the outmost layer cross-validation structure in RapidMiner.

Table 5.2 Result of Calssification

	Sensitivity	Specificity	Accuracy
mean value	68.6	76.6	73.7
standard deviation	7.3	3.9	4.2

After feature selection, 10 fold cross validation is implemented three times with random split of the data. Table 5.2 shows the result of classification. The total classification accuracy is around 74% in predicting ICP levels. The result shows promise towards developing a viable ICP prediction tool.

5.3.3 Discussion

Selected features in each fold may be different because of the random/different training data. Thus a vote operation based on the frequency of occurrence is applied the 10 fold cross validation on all selected features gathered from 10 feature set. Around 30 features are extracted from each fold. The features with low frequency of occurrence are removed before classification. It is noticed that around 12 features in each fold are unique due to a limited dataset. The selected feature set mainly belongs to texture features because of the

high proportion of texture feature 87% (220/252). The features, such as ventricle size and intracranial air, are also selected.

5.4 Summary

In this work, an ICP level prediction model is proposed and validated using machine learning method. Multiple features, such as midline shift, intracranial air cavities, ventricle size, texture patterns, and blood amount are extracted automatically from the brain CT images using advanced image processing methods. In addition demographic information such as age and ISS are also used as candidate features. To avoid over fitting, the model is validated based on nested 10 fold cross validation. The obtained results show that the proposed model can potentially be applied towards developing a prediction system for physician in medical decision making.

Chapter 6: Summary

This research provides a framework of the automated midline shift estimation system on brain CT images for computer-aided decision support. Two novel algorithms, namely CT Slice Selection Algorithm (SSA) and Window Selection Algorithm (WSA), have been designed to select appropriate CT slice and confine region of interest for midline detection. Exhaustive searching associated with global rotation method are utilized in ideal midline detection. Variational level set method implements image segmentation to extract ventricle contours for actual midline detection. If implemented as a clinical diagnostic tool, the fully automated process could significantly reduce the diagnosis time.

In the slice selection step, the SSA algorithm closely simulates the process of manual CT slice selection by physicians in clinical practice. Fully considering the anatomical characteristics of the brain and the need for midline shift estimation, SSA selects the CT images with closed skull, large intracranial area, good convexity, and clear ventricle information. To quantitatively measure the above features, a series of new measures are proposed in this work, including skull closing level F, total intracranial convex measure Λ_{Total} , and ventricle fidelity measure F_v. Each slice in one brain CT scan is examined step by step using the above measures. Finally, the most appropriate few slices (around 10% slices are selected in this work) are selected for the following midline detection. The great reduction in the number of slices ensure a computation time saving for the system.

The designed ideal midline detection process fully considers the symmetry of the skull and anatomical features in the identification of IML on the slices selected by the SSA algorithm. Based on row symmetry cost, an exhaustive symmetric position search method is used to detect the approximate position of IML. Subsequently, using the brain

anatomical features, such as the position of the falx cerebri and protrusion of skull bone, the position of IML is refined. The application of global rotation on both steps ensures the connection among CT slices being fully considered and thereby the error generated by using a single CT slice being compensated. Finally, the calibrated IML and the aligned image provide a foundation for the following actual midline detection and midline shift estimation. Comparing with the work of other research group, our system yields a high accuracy after the test on a large database.

In the actual midline detection step, variational level set segmentation method associated with window selection algorithm, weighted median filter, and ventricle validation process is designed to detect the position of the actual midline. For the purpose of saving computation time in segmentation, window selection algorithm (WSA) is proposed to select the most appropriate slice and confine the window only to the ventricle area. The new measure, window selection measure F_w, is used to quantitatively evaluate the quality of selected window containing ventricle information. WSA greatly enhances the efficiency of the whole system by reducing segmentation time. In addition, the window selected by WSA is used as the initialization for the segmentation. Variational level set method is very popular in the medical image processing. As the first attempt to apply this method in MLS estimation, the utilization of variational level set segmentation successfully extracts ventricle contours and provides the crucial index for the actual midline detection. Using the positions of ideal midline and actual midline, the midline shift is accurately estimated. With a strict definition of accuracy, our system achieves a desirable high accuracy of 92.5% in the actual midline estimation.

As an important application of midline shift estimation in clinical setting, an ICP level prediction model is designed and validated using machine learning method. In order to implement the classification in ICP prediction, multiple features, such as midline shift, intracranial air cavities, ventricle size, texture patterns, and blood amount are extracted automatically from the brain CT images using advanced image processing methods. The aggregated features of the above features are also utilized in the classification model. In addition demographic information such as age and ISS are also used as candidate features. The results obtained by support vector machine show that the proposed model can potentially be applied towards developing a prediction system for physician in medical decision making.

References

[1] M. Faul, L. Xu, M. M. Wald, and V. G. Coronado, "Traumatic Brain Injury in the United States: Emergency Department Visits, Hospitalizations, and Deaths", *Centers for Disease Control and Prevention, National Center for Injury Prevention and Control*, Atlanta, GA, USA, 2010.

[2] M. R. Hemmila, J. L. Jakubus, P. M. Maggio, W. L. Wahl, J. B. Dimick, D. A. Campbell, and P. A. Taheri, "Real money: complications and hospital costs in trauma patients," *Surgery*, vol. 144, no.2, pp. 307-316, 2008

[3] K. Kendall-Tackett, "Psychological trauma and physical health: a psychoneuroimmunology approach to etiology of negative health effects and possible interventions" *Psychological Trauma: Theory, Research, Practice and Policy*, vol. 1, no. 1, pp.35-48, 2009

[4] J. A. Depalma, P. Fedorka, and L. C. Simko, "Quality of life experienced by severely injured trauma survivors," *AACN Clinical Issues*, vol. 14, no. 1, pp.54-63, 2003

[5] T. Novack, "TBI Inform - Introduction to Brain Injury: Facts & Stats," *UAB-TBIMS*, Birmingham, AL, USA, 2000

[6] A. Lavinio and D. K. Menon, "Intracranial pressure: why we monitor it, how to monitor it, what to do with the number and what's the future?" *Curr. Opin. Anesthesiol.*, vol. 24, No.2, pp.117-123, 2011

[7] H. T. Stelfox, B. Bobranska-Artiuch, A. nathens, and S. E. Straus, "Quality indicators for evaluating trauma care," *Arch. Surg*., vol.145, no. 3, pp.286-295, 2010

[8] T. Geeraerts, V. Chhor, G. Cheisson, L. Martin, B. Bessoud, A. Ozanne, J. Duranteau, "Clinical review: initial management of blunt pelvic trauma patients with haemodynamic instability," *Critical Care*, vol. 11, no. 1, pp. 204, 2007

[9] W. Chen, R. Smith, S.Y. Ji, K. Ward, and K. Najarian, "Automated ventricular systems segmentation in brain CT images by combining low-level segmentation and high-level template matching," *BMC Medical Informatics and Decision Making*, vol. 9, no. 1, 2009

[10] J. S. Broder, "Head computed tomography interpretation in trauma: a primer," The Psychiatric Clinics of North America, vol. 33, pp. 821–854, 2010

[11] http://www.mybwmc.org/library/3/100123

[12] http://www.wired.com/gadgets/miscellaneous/news/2008/04/Toshiba_CTScanner

[13] E. E. Moore, D. V. Feliciano, and K. L. Mattox, "Trauma," *McGraw-Hill Professional*, 5 edition, October 2003

[14] Merriam-Webster Online Dictionary, http://www.merriamwebster.com/dictionary/computed+tomography, 2009

[15] K. Subburaj, "CT Scanning - Techniques and Applications," *In Tech*, Chapter 9, 2011

[16] S. R. Shackford, S. L. Wald, S. E. Ross, T. H. Cogbill, D. B. Hoyt, J. A. Morris, P. A. Mucha, H. L. Pachter, H. J. Sugerman, K. O'Malley, "The clinical utility of computed tomographic scanning and neurologic examination in the management of patients with minor head injuries," *J Trauma*, vol. 33, no. 3, pp 385-394, 1992

[17] S. C. Stein and S. E. Ross, "The value of computed tomographic scans in patients with low-risk head injuries," *Neurosurgery*, vol. 26, no. 4, pp 638-640, 1990

[18] S. C. Stein and S. E. Ross, "Minor head injury: a proposed strategy for emergency management," *Ann Emerg Med*, vol. 22, no. 7, pp 1193-1196, 1993

[19] http://www.radiologyinfo.org/en/info.cfm?pg=bodyct

[20] P. Shreve and D. W. Townsend, "Clinical Pet-Ct In Radiology: Integrated Imaging In Oncology" *Springer*, Chapter 1, 2011

[21] http://emedicine.medscape.com/article/1923254-overview

[22] "Medical Dictionary," 3rd Edition, *Webster's New World*, May, 2008

[23] http://www.mybwmc.org/library/3/100123

[24] R. R. Ivatury, K. Guilford, A. K. Malhotra, T. Duane, M. Aboutanos, and N. Martin, "Patient Safety in Trauma: Maximal impact management errors at a level I trauma center," *J. Trauma*, vol. 64, no. 2, pp.265-272, 2008

[25] R. L. Gruen, G. J. Jurkovich, L. K. McIntyre, H. M. Foy, and R. V. Maier, "Patterns of errors contributing to trauma mortality: lessons learned from 2594 deaths," *Ann. Surg.*, vo.l 244, no. 3, pp.371-380, 2006

[26] K. Kahol, M. Vanikpuram, V. L. Patel, and M. L. Smith, "Deviations from protocol in a complex trauma environment: errors or innovations?" *Journal of Biomedical Informatics*, vol. 44, pp.425-431, 2011

[27] M. Fitzgerald, P. Cameron, C. Mackenzie, N. Farrow, P. Scicluna, R. Gocentas, A. Bystrzycki, G. Lee, G. O'Reilly, N. Andrianopoulos, L. Dziukas, D. J. Cooper, A. Silvers, A. Mori, A. Murray, S. Smith, Y. Xiao, D. Stub, F. T. McDermott, J. V. Rosenfeld, "Trauma Resuscitation eroors and computer-assisted decision support," *Arch. Of Surgery*, vol. 146, no.2, pp. 218-225, 2011

[28] Laxmisan, F. hakimzada, O. R. Sayan, R. A. Green, J. Zhang, V. L. Patel, "The multitasking clinician: decision-making and cognitive demand during and after team handoffs in emergency care," *International journal of Medical Informatics*, vol. 76, pp. 801-811, 2007

[29] K. D. stahl and S. E. Brien, "Reducing patient errors in trauma care," In: *Cohn S, ed. Acute care Surgery*: *Evidenced-based practice*. New York, NY: Informa Healthcare USA Inc., pp. 268-277, 2009

[30] K. D. Stahl, A. Palileo, C. I. Schulman, K. Wilson, J. Augenstein, C. Kiffin, M. McKenney, "Enhancing patient safety in the trauma/surgical intensive care unit," *J. Trauma*, vol. 67, no. 3, pp. 430-435, 2009

[31] D. L. Pham, C. Xu, and J. Prince, "Current methods in medical image segmentation," Annu. Rev. Biomed., vol. 2, pp. 315-337, 2000

[32] L. G. Shapiro and G. C. Stockman, "Computer Vision," pp. 279-325, 2001

[33] A. A. Othman, H. R. Tizhoosh, "Evolving fuzzy image segmentation," *Fuzzy Systems (FUZZ), 2011 IEEE International Conference on* , pp.1603-1609, Jun. 2011

[34]S. M. Larie and S. S. Abukmeil, "Brain abnormality in schizophrenia: a systematic and quantitative review of volumetric magnetic resonance imaging studies," *J. Psych.*, vol. 172, pp. 110–120, 1998

[35] P. Taylor, "Invited review: computer aids for decision-making in diagnostic radiology— a literature review," *Brit. J. Radiol.*, vol. 68, pp. 945–957, 1995

[36] A. P. Zijdenbos and B. M. Dawant, "Brain segmentation and white matter lesion detection in MR images," *Crit. Rev. Biomed. Eng.*, vol. 22, pp.401–465, 1994

[37] A. J. Worth, N. Makris, V.S. Caviness, and D. N. Kennedy, "Neuroanatomical segmentation in MRI: technological objectives," *Int. J. Patt. Rec. Art. Intel.*, vol.11, pp.1161–1187, 1997

[38] V. S. Khoo, D. P. Dearnaley, D. J. Finnigan, A. Padhani, S. F. Tanner, and M. O. Leach, "Magnetic resonance imaging (MRI): considerations and applications in radiotheraphy treatment planning," *Radiother. Oncol.*, vol. 42, pp.1–15, 1997

[39] H. W. Muller-Gartner, J. M. Links, J. L. Prince, R. N. Bryan, E. McVeigh, J. P. Leal, C. Davatzikos, J. J. Frost, "Measurement of radiotracer concentration in brain gray matter using positron emission tomography: MRI-based correction for partial volume effects," *J. Cereb. Blood Flow Metab.*, vol. 12, pp.571–583, 1992

[40] N. Ayache, P. Cinquin, I. Cohen, L. Cohen, F. Leitner, and O. Monga, "Segmentation of complex threedimensional medical objects: a challenge and a requirement for computer-assisted surgery planning and performance," *Computerintegrated surgery: technology and clinical applications*, pp. 59-74, 1996

[41] W. E. L. Grimson, G. J. Ettinger, T. Kapur, M. E. Leventon, W. M. Wells, R. Kikinis, "Utilizing segmented MRI data in image-guided surgery," *Int. J. Patt. Rec. Art. Intel.*, vol. 11, pp.1367-1397, 1997

[42] R. Kountchev and K. Nakamatsu, "Advances in Reasoning-Based Image Processing Intelligent Systems," *Springer*, pp. 133, 2012

[43] R. C. Gonzalez and R. E. Woods, "Digital Image Processing," *Prentice Hall*, 2 edition, 2002

[44] R. M. Haralick and L. G. Shapiro, "Image segmentation techniques," *Comput. Vis.Graph. Im. Proc.*, vol. 29, pp. 100–132, 1985

[45] Z. Peter, V. Bousson, C. Bergot, and F. Peyrin, "A constrained region growing approach based on watershed for the segmentation of low contrast structures in bone micro-CT images", *Pattern Recognition*, vol.41, no.7, pp. 2358-2368, 2008

[46] Z. Ma, J. M. Tavares, R. N. Jorge, and T. Mascarenhas, "A review of algorithms for medical image segmentation and their applications to the female pelvic cavity," *Comput Methods Biomech Biomed Engin.*, vol. 13, no. 2, pp. 235-46, 2010

[47] T. Heimann, B. Van Ginneken, M. A. Styner, Y. Arzhaeva, V. Aurich, *et al.*, "Comparison and evaluation of methods for liver segmentation from CT datasets," *IEEE Trans. On Medical Imaging*, vol. 28, no. 8, pp. 1251-1265, 2009

[48] J. C. Dunn, "A fuzzy relative of the ISODATA process and its use in detecting compact well-sparated clusters," *Journal of Cybernetics*, vol. 3, pp. 32–57, 1973

[49] Z. Liang, J. R. MacFall, and D. P. Harrington, "Parameter estimation and tissue segmentation from multispectral MR images," *IEEE T. Med. Imag.*, vol.13, pp.441–449, 1994

[50] J. C. Rajapakse, J. N. Giedd, and J. L. Rapoport, "Statistical approach to segmentation of single-channel cerebral MR images," *IEEE T. Med. Imag.*, vol. 16, pp. 176–186, 1997

[51] S. N. Jha, "Nondestructive evaluation of food quality," *Springer*, pp. 187, 2010

[52] T. Lei and W. Sewchand, "Statistical approach to x-ray ct imaging and its applications in image analysis. i. statistical analysis of x-ray ct imaging," *IEEE Trans Med Imaging*, vol.11, No.1, pp. 53–61, 1992

[53] C. Carson, S. Belongie, H. Greenspan, and J. Malik, "Blobworld: Image segmentation using expectation-maximization and its application to image querying," *IEEE Transactions on Pattern Analysis and Machine Intelligence*, vol. 24, pp. 1026–1038, 2002

[54] H. Greenspan, A. Ruf, and J. Goldberger, "Constrained gaussian mixture model framework for automatic segmentation of MR brain images," *IEEE Trans. Med. Imaging*, vol. 25, No.9, pp.1233–1245, 2006

[55] L. I Kuncheva and L. C Jain, "Nearest neighbor classifier: Simultaneous editing and feature selection," *Pattern Recognition Letters*, vol. 20, no. 11–13, pp. 1149–1156, 1999

[56] T. Denoeux, "A k-nearest neighbor classification rule based on Dempster-Shafer theory," *IEEE Transactions on Systems, Man and Cybernetics*, vol. 25, no. 5, pp. 804-813, 1995

[57] J. Aldrich, "R. A. Fisher and the making of maximum likelihood 1912–1922," *Statist. Sci.*, vol. 12, no. 3, pp.162–176, 1997

[58] C. Xu, D. L. Pham, and J. L. Prince, "Medical Image Segmentation Using Deformable Models," Handbook of Medical Imaging, Vol. 2: Medical Image Processing and Analysis, *SPIE Press*, pp. 129-174, May 2000

[59] Z. Hui, E.F. Jason, and A.G. Sally, "Image segmentation evaluation: a survey of unsupervised methods", *Computer Vision and Image Understanding*, vol. 110, no. 2, pp. 260–280, 2008

[60] Y. J. Zhang, "A survey on evaluation methods for image segmentation," *Pattern Recognition*, vol. 29, no. 8, pp. 1335–1346, 1996

[61] D. R. Martin, C. C. Fowlkes, J. Malik, "Learning to detect natural image boundaries using local brightness, color, and texture cues," *IEEE Transactions on Pattern Analysis and Machine Intelligence*, vol. 26, no. 5, pp. 530–549, 2004

[62] A. M. Bensaid, L. O. Hall, J. C. Bezdek, and L. P. Clarke, "Validity-guided (re)clustering with applications to image segmentation," *IEEE Transactions on Fuzzy Systems*, vol. 4, no. 2, pp. 112–123, 1996

[63] M. C. Shin, D. B. Goldgof, and K. W. Bowyer, "Comparison of Edge Detector Performance Through Use in an Object Recognition Task," *Computer Vision and Image Understanding*, vol. 84, no.1, pp. 160-178, 2001.

[64] M. C. Shin, D. B. Goldgof, K. W. Bowyer, and S. Nikiforou, "Comparison of Edge Detector Algorithms Using a Structure from Motion Task," *IEEE Trans. Systems, Man and Cybernetics Part B: Cybernetics*, vol. 31, no. 4, pp. 589-601, 2001.

[65] L. Yang, F. Albregtsen, T. Lonnestad, and P. Grottum, "A supervised approach to the evaluation of image segmentation methods," *Computer Analysis of Images and Patterns*, vol. 970, pp. 759-765, 1995

[66] S. Chabrier, H. Laurent, B. Emile, C. Rosenburger, and P. Marche, "A comparative study of supervised evaluation criteria for image segmentation," *EUSIPCO*, pp. 1143-1146, 2004

[67] P. Correia and F. Pereira, "Objective evaluation of relative segmentation quality," Image Processing, vol. 1, pp. 308-311, 2000

[68] C. Graaf, A. Koster, K. Vincken, and M. Viergever, "Validation of the interleaved pyramid for the segmentation of 3d vector images," *Pattern Recognition Letters*, vol. 15, pp. 467-475, 1994

[69] W. A. Yasnoff, J. K. Mui, and J. W. Bacus, "Error measure for scene segmentation," *Pattern Recognition*, vol. 9, pp. 217-231, 1977

[70] J. Weszka and A. Rosenfeld, "Threshold evaluation techniques," *IEEE Transactions on Systems, Man and Cybernetics*, vol. 8, no. 8, pp. 622-629, Aug. 1978

[71] S. Lee, S. Chung, and R. Park, "A comparative performance study of several global thresholding techniques for segmentation," *Computer Vision, Graphis, and Image Processing*, vol. 52, pp. 171-190, 1990

[72] Y. Lim and S. Lee, "On the color image segmentation algorithms based on the thresholding and fuzzy c-means techniques," *Pattern Recognition*, vol. 23, pp. 935-952, 1990

[73] M. Wollborn and R. Mech, "Refined procedure for objective evaluation of video generation algorithms," *43rd MPEG Meeting*, March 1998

[74] K. Strasters and J. Gerbrands, "Three-dimensional image segmentation using split, merge and group approach," Pattern Recognition Letters, vol. 12, pp. 307-325, 1991.

[75] N. Pal and D. Bhandari, "Image thresholding: some new techniques," *Signal Processing*, vol. 33, no. 2, pp. 139-158, Aug. 1993

[76] Y. Zhang and J. Gerbrands, "Objective and quantitative segmentation evaluation and comparison," Signal Processing, vol. 39, pp. 43-54, 1994

[77] P. Correia and F.Pereira, "Objective evaluation of video segmentation quality," *IEEE Transactions on Image Processing*, vol. 12, no. 2, pp. 186-200, Feb. 2003

[78] M. Van Droogenbroeck and O. Barnich, "Design of Statistical Measures for the Assessment of Image Segmentation Schemes", *Proc. of the 11th International Conference on Computer Analysis of Images and Patterns*, pp. 280-287, 2005

[79] F. Ge, S. Wang, and T. Liu, "Image-Segmentation Evaluation From the Perspective of Salient Object Extraction", *Proc. of IEEE Internatioanl Conference on Computer Vision and Pattern Recognition*, Vol 1, pp. 1146-1153, 2006

[80] T. Kanungo, M. Jaisimha, J. Palmer, and R. M. Haralick, "A methodology for quantitative performance evaluation of detection algorithms," *IEEE Transactions on Image Processing*, vol. 4, no. 12, pp. 1667-1673, Dec. 1995

[81] K. Bowyer, C. Kranenburg and S. Dougherty, "Edge detector evaluation using empirical roc curves," *Computer Vision and Image Understanding*, vol. 84, no. 1, pp. 77-103, Oct. 2001

[82] D. Pavani, W. Jie, T. Yang, C. Charles, W. Kevin, N. Kayvan, and Rosalyn H. Hargraves, "Hemorrhage Detection and Segmentation in Traumatic Pelvic Injuries", *Comput. Math Methods Med*, Vol. 2012, 898430, 2012

[83] W. Chen, R. Smith, S.Y. Ji, and K. Najarian, "Automated segmentation of lateral ventricales in brain CT images" *Bioinformatics and Biomeidcine Workshops, IEEE International Conference*, pp. 48-55, 2008

[84] Haralick, Robert M., and Linda G. Shapiro, "Computer and Robot Vision," Volume I, pp. 28-48, 1992

[85] P. K. Woodrow, J. Gajarawala, J. Yaghoobian, and R. L. Pinck, "CT detection of subarachnoid pneumocephalus secondary to mastoid fracture," *J Comput Tomogr*., Vol. 5, No.2, pp. 199-201, 1981

[86] T. Sloan, "The incidence, volume, absorption, and timing of supratentorial pneumocephalus during posterior fossa neurosurgery conducted in the sitting position," *J Neurosurg Anesthesiol*, Vol. 22, No.1, pp. 59-66, 2010

[87] O. N. Syed, D. Weintraub, R. DeLaPaz, E. S. Connolly, "Venous air emboli from intravenous catheterization: a report of iatrogenic intravascular pneumocephalus," *J Clin Neurosci*, Vol. 16, No. 10, pp. 1361-1362, 2009

[88] G. C. S. Ruppert, L. Teverovskiyz, C. Yu, A. X. Falcao, and Y. Liu, "A New Symmetry-based Method for Mid-sagittal Plane Extraction in Neuroimages," *IEEE International Symposium on Biomedical Imaging: From Nano to Macro*, pp. 285-288, 2011

[89] Q. Hu and W. L. Nowinski, "A rapid algorithm for robust and automatic extraction of the midsagittal plane of the human cerebrum from neuroimages based on local symmetry and outlier removal," *NeuroImage* 20, No.4, pp. 2153–2165, 2003

[90] C.C. Liao, F. Xiao; J. Wong, and I. Chiang, "A simple genetic algorithm for tracing the deformed midline on a single slice of brain CT using quadratic Bezier curves," *Sixth IEEE International Conference on Data Mining Workshops*, 2006, pp. 463-467

[91] F. P. G. Bergo, G. C. S. Ruppert, and A. X. Falcao, "Fast and robust mid-sagittal plane location in 3D MR images of the brain," *International Conference on Bioinspired Systems and Signal Processing*, pp. 92-99, 2008

[92] R. Guillemaud, P. Marais, A. Zisserman, B. McDonald, T. J. Crow, and M. Brady, "A three dimensional mid sagittal plane for brain asymmetry measurement," *Schizophrenia Research* , vol. 18, No. 2, pp. 183–184, 1996

[93] G. Ruppert, L. Teverovskiy, C. Yu, A. Falcao, and Y. Liu, "A New Symmetry-Based Method For Mid-Sagittal Plane Extraction In Neuroimages," *IEEE International Symposium on Biomedical Imaging (ISBI)*, pp. 285-288, 2011

[94] L. Teverovskiy and Y. Liu, "Truly 3D midsagittal plane extraction for robust neuroimage registration," *The 3rd IEEE Intl. Symp. on Biomedical Imaging*, pp. 860–863, 2006

[95] W. Chen and K. Najarian, "Segmentation of ventricles in brain CT images using Gaussian mixture model method," *Proceedings of IEEE International Conference on Complex Medical Engineering (CME),* pp. 1-6, Apr. 2009

[96] C.C. Liao, I.J. Chiang, F. Xiao, and J.M. Wong, "Tracing the deformed midline on brain CT," *Biomedical Engineering Application, Basis and Communications*, vol. 18, pp. 305-311, Dec. 2006

[97] R. Liu, S. Li, C. L. Tan, B. C. Pang, C. C. T Lim, C. K. Lee, Q. Tian, Z. Zhang, "From hemorrhage to midline shift: A new method of tracing the deformed midline in traumatic brain injury ct images," *16th IEEE International Conference on Image Processing*, pp. 2637-2640, 2009

[98] M. Kass, A.Witkin, and D. Terzopoulos, "Snakes: active contour models", *International Journal of Computer Vision*, vol. 1, pp. 321-331, 1987

[99] S. Kichenassamy , A. Kumar , P. Olver , A. Tannenbaum and A. Yezzi "Gradient flows and geometric active contour models", *Proc. 5th Int. Conf. Comput. Vis.*, pp.810 - 815, 1995

[100] A. Yezzi, S. Kichenassamy, A. Kumar, P. Olver, and A. Tannenbaum, "A geometric snake model for segmentation of medical imagery," *IEEE Trans. Med. Imag.*, vol. 16, pp. 199–209, Apr. 1997.

[101]A. Gupta, L. von Kurowski, A. Singh, D. Geiger, C. Liang, M. Chiu, P. Adler, M. Haacke, and D. Wilson, "Cardiac MRI analysis: Segmentation of myocardial boundaries using deformable models," *Siemens Corp. Res., Princeton*, NJ, Tech. Rep., 1995

[102] S. Raganath, "Contour extraction from cardiac MRI studies using snakes," *IEEE Trans. Med. Imag.*, vol. 14, pp. 328–338, 1995

[103] S. Kichenassamy, A. Kumar, P. Olver, A. Tannenbaum, and A. Yezzi, "Gradient flows and geometric active contours," *Proc. ICCV*, Jun. 1995

[104] C. M. Chen, H. H. S. Lu, and Y .C. Lin, "An early vision based snake model for ultrasound image segmentation," *Ultrasound Med Biol*, vol. 26, no. 2, pp. 273–285, 2000

[105] V. Chalana, D. T. Linker, D.R. Haynor, and Y. Kim "A multiple active contour model for cardiac boundary detection on echocardiographic sequences," *IEEE Trans Med Imaging*, vol. 15, pp. 290–298, 1996

[106] H.-K. Zhao, S. Osher, B. Merriman, and M. Kang, "Implicit, nonparametric shape reconstruction from unorganized data using a variational level set method," *Computer Vision and Image Understanding*, vol. 80, no. 3, pp. 295-314, 2000

[107] L. A. Vese and T. F. Chan, "A Multiphase Level Set Framework for Image Segmentation Using the Mumford and Shah Model," *International Journal of Computer Vision*, vol. 50, no. 3, pp. 271–293, 2002

[108] T. Chan and L. Vese, "Active contours without edges", *IEEE Trans. Image. Process.*, vol. 10, no. 2, pp. 266 -277, 2001

[109] R. Ronfard, "Region-based strategies for active contour models," *Int. J. Comput. Vis.*, vol. 13, no. 2, pp. 229 -251, 1994

[110] A. Tsai , A. Yezzi, and A. S. Willsky, "Curve evolution implementation of the Mumford-Shah functional for image segmentation, denoising, interpolation, and magnification," *IEEE Trans. Image Process.*, vol. 10, no. 8, pp.1169 -1186, 2001

[111] V. Caselles, R. Kimmel, G. Sapiro, "Geodesic Active Contours," *International Journal of Computer Vision*, vol. 22, no. 1, pp.61-79, 1997

[112] L. M. Lorigo, O. Faugeras , W. E. L. Grimson, R. Keriven, R. Kikinis, A. Nabavi, and C. F. E. Westin, "Codimension-two geodesic active contours for the segmentation of tubular structures," *IEEE Conference on Computer Vision and Pattern Recognition*, vol.1, pp.444-451, 2000

[113] N. Paragios, "A level set approach for shape-driven segmentation and tracking of the left ventricle," *IEEE Transactions on Medical Imaging*, vol.22, no.6, pp. 773-776, 2003

[114] S. Chen, D. M. Lovelock, and R. J. Radke. "Segmenting the prostate and rectum in CT imagery using an atomical constraints," *Medical Image Analysis*, Vol. 15, No.1, pp. 1-11, 2011

[115] V. Caselles, F. Catte, T. Coll, and F. Dibos, "A geometric model for active contours in image processing," *Numerische Mathematik*, vol. 66, no. 1, pp. 1–31, 1993

[116] R. Malladi, J. A. Sethian, and B. C. Vemuri, "Shape modeling with front propagation: a level set approach", *IEEE Transactions on Pattern Analysis and Machine Intelligence*, vol. 17, no. 2, pp. 158-175, Feb. 1995

[117] S. Osher and J. Sethian, "Fronts propagating with curvature-dependent speed: Algorithms based on Hamilton-Jacobi formulations," *Journal of Computational Physics*, vol. 79, no. 1, pp. 12–49, 1988

[118] B. B. Kimia, A. Tannenbaum, and S. Zucker, "Shapes, shocks, and deformations I: the components of two dimensional shape and the reaction-diffusion space", *International Journal of Computer Vision*, vol. 15, pp. 189-224, 1995

[119] C. Li, C. Xu, C. Gui, and M. D. Fox, "Level Set Evolution Without Re-initialization: A New Variational Formulation", *Computer Vision and Pattern Recognition,* vol. 1, pp. 430-436, 2005

[120] C. Li, C. Kao, J. C. Gore, and Z. Ding, "Minimization of Region-Scalable Fitting Energy for Image Segmentation", *IEEE Transactions on Image Processing*, vol. 17, no. 10, pp. 1940-1949, 2008

[121] C. Li, R. Huang, Z. Ding, C. Gatenby, D. N. Metaxas, and J. C. Gore, "A Level Set Method for Image Segmentation in the Presence of Intensity Inhomogeneities with Application to MRI", *IEEE Transactions on Image Processing* , vol. 20, no.7, pp. 2007-2016, Jul. 2011

[122] T. Loupas, W. N. McDicken, and P. L. Allan, "An adaptive weighted median filter for speckle suppression in medical ultrasonic images," *IEEE Trans. Circ. Sysr.*, vol. 36, pp. 129-135, Jan. 1989

[123] L. Yin, J. Astola, and Y. Neuvo, "Adaptive stack filtering with application to image processing," *IEEE Trans. Signal Processing*, vol. 41, pp. 162-184, Jan. 1993

[124] B. Alp, J. Juhola, Y. Neuvo, and T. Jarske, "Multidimensional reconstruction of quincunx coded image sequences," *Proc. Picture Coding Symp.*, Cambridge, MA, pp. 735, Mar. 1990

[125] B. J. Justusson, "Median filtering: Statistical properties," *Two Dimensional Digital Signal Processing II*, Berlin: Springer-Verlag, vol. 43, pp. 161-196, 1981

[126] R. Yang, L. Yin, M. Gabbouj, J. Astola, and Y. Neuvo, "Optimal weighted median filters under structural constraints," *IEEE Trans. Signal Processing*, vol. 43, pp. 591–604, Mar. 1995

[127] Y. Fei and J. W. Park, "A New Variational Level Set Evolving Algorithm for Image Segmentation," Journal of Information Processing Systems, vol.5, no.1, pp. 1-4, 2009

[128] H. Zhao, T. Chan, B. Merriman, and S. Osher, "A Variational Level Set Approach to Multiphase Motion," *J. Comp. Phys.*, vol.127, pp. 179-195, 1996

[129] A. R. Deepak, T. Le, V. Bhushan, "First Aid for the USMLE Step 1 2008," *McGraw-Hill Medical*, pp. 254, 2007

[130] R. J. Forsyth, S. Wolny, and B. Rodrigues, "Routine intracranial pressure monitoring in acute coma," *Cochrane Database Syst Rev.*, vol. 17, no. 2, 2010

[131] S. H. Haddad and M. A. Yaseen, "Critical care management of severe traumatic brain injury in adults," *Scand. J. Trauma Resusc. Emerg. Med.*, vol. 20, no. 1, pp. 12, 2012

[132] W. Chen, C. Cockrell, K. R. Ward, and K. Najarian, "Intracranial pressure level prediction in traumatic brain injury by extracting features from multiple sources and using machine learning methods," *2010 IEEE International Conference on Bioinformatics and Biomedicine*, pp. 510-515, Dec. 2010

[133] D. I. Graham and T. A. Gennareli, "Pathology of Brain Damage After Head Injury" Chapter 5, *Cooper P and Golfinos G. 2000. Head Injury*, 4th Ed. Morgan Hill, New York

[134] W. Chen and K. Najarian, "Segmentation of Ventricles in Brain CT Images Using Gaussian Mixture Model Method," *Proceedings of IEEE International Conference on Complex Medical Engineering*, pp. 15–20, Apr. 2009

[135] S. A. Kabara, M. Gabbouj, P. Dastidar, F. A. Cheikh, P. Ryymin, and E. Laasonen, "Ct image texture analysis of intracerebral hemorrhage," *Proceedings of the 2003 Finnish Signal Processing Symposium*, FINSIG'03, pp. 190–194, 2003

[136] A. E. Svolos and A. Todd-Pokropek, "Time and space results of dynamic texture feature extraction in mr and ct image analysis," *IEEE Trans Inf Technol Biomed*, vol. 2, no. 2, pp. 48–54, 1998

[137] R. W. Conners and C. A. Harlow, "A theoretical comparison of texture algorithm," *IEEE Trans. on Pattern Analysis and Machine Intelligence*, vol. PAMI-2, No. 3, pp. 204–222, 1980

[138] H. Peng, F. Long, and C. Ding, "Feature Selection Based on Mutual Information: Criteria of Max-Dependency, Max-Relevance, and Min-Redundancy," *IEEE Trans. on Pattern Analysis and Machine Intelligence*, vol. 27, no. 8, pp. 1226–1238, Aug. 2005

[139] I. Mierswa, M. Wurst, R. Klinkenberg, M. Scholz, and T. Euler, "Yale: Rapid prototyping for complex data mining tasks," *KDD '06: Proceedings of the 12th ACM SIGKDD international conference on Knowl-edge discovery and data mining*, NY, USA, pp. 935–940, Aug. 2006